J. Fluid Mech. (1986), *vol.* 163, *pp.* 69–98
Printed in Great Britain

Calculations of self-excited impinging jet flow

By SAMUEL OHRING
David W. Taylor Naval Ship Research and Development Center,
Bethesda, Maryland 20084

(Received 15 January 1985 and in revised form 30 April 1985)

This paper presents numerical calculations of the self-excited oscillations of an incompressible planar jet impinging upon a wedge for a Reynolds-number range of 250–650. For this Reynolds-number range these flows are experimentally observed to be two-dimensional and laminar. A finite-difference vorticity/stream-function formulation of the Navier–Stokes equations is employed. The self-sustained flow oscillations result in not just one but several well-defined flow frequency components due to nonlinear interaction of two primary components: the most unstable frequency (β) of the jet shear layer and a low-frequency modulating component ($\frac{1}{3}\beta$). The modulating component results from vortex–vortex interaction at the impingement edge of both like and counter-rotating vortices. Although the interaction pattern varies through the Reynolds-number range studied, the pattern adjusts itself to maintain the modulating component $\frac{1}{3}\beta$ which has a strong upstream influence. The numerical results, in agreement with experimental results, strongly suggest the occurrence of such phenomena as frequency jumps and hysteresis. Pressure at the wedge surface has been calculated and compared with experimental results. Numerical results for wedge torque and lift, which have not been experimentally measured, have also been obtained.

1. Introduction

Significant advancement in understanding the impingement of a planar jet upon an edge has resulted from the earlier theoretical investigations of Powell (1961) and the more recent investigations summarized by Rockwell (1983). Therefore, it is well known that impingement of a planar jet upon an edge can give rise to strongly coherent, self-sustained oscillations whose main features are schematically displayed in figure 1 (*a*). These features are (*i*) amplification of unstable disturbances in the shear layer of the jet associated with a downstream travelling instability wave, (*ii*) impingement of this amplified disturbance (i.e. vorticity field) upon the wedge, (*iii*) feedback or upstream influence of this unsteady interaction at the impingement edge and (*iv*) conversion of this feedback to vorticity fluctuations in the sensitive region of the shear layer near the nozzle opening. The entire cycle then repeats with the latest vorticity fluctuations being amplified and so on.

One of the most interesting aspects of jet-edge flows was discussed in detail by Powell (1961) and more recently by Rockwell (1983). These jet-edge flows exhibit jumps in oscillation frequency as well as hysteresis, when the impingement length (the distance from the nozzle opening to the wedge tip) or the average velocity U of the nozzle flow is varied. Figure 1 (*b*) schematically represents these upward and downward jumps in frequency f and the associated hysteresis loop for the case where the flow velocity U is first increased, then decreased, as indicated by the arrows. An inherent assumption in nearly all theoretical and experimental investigations carried

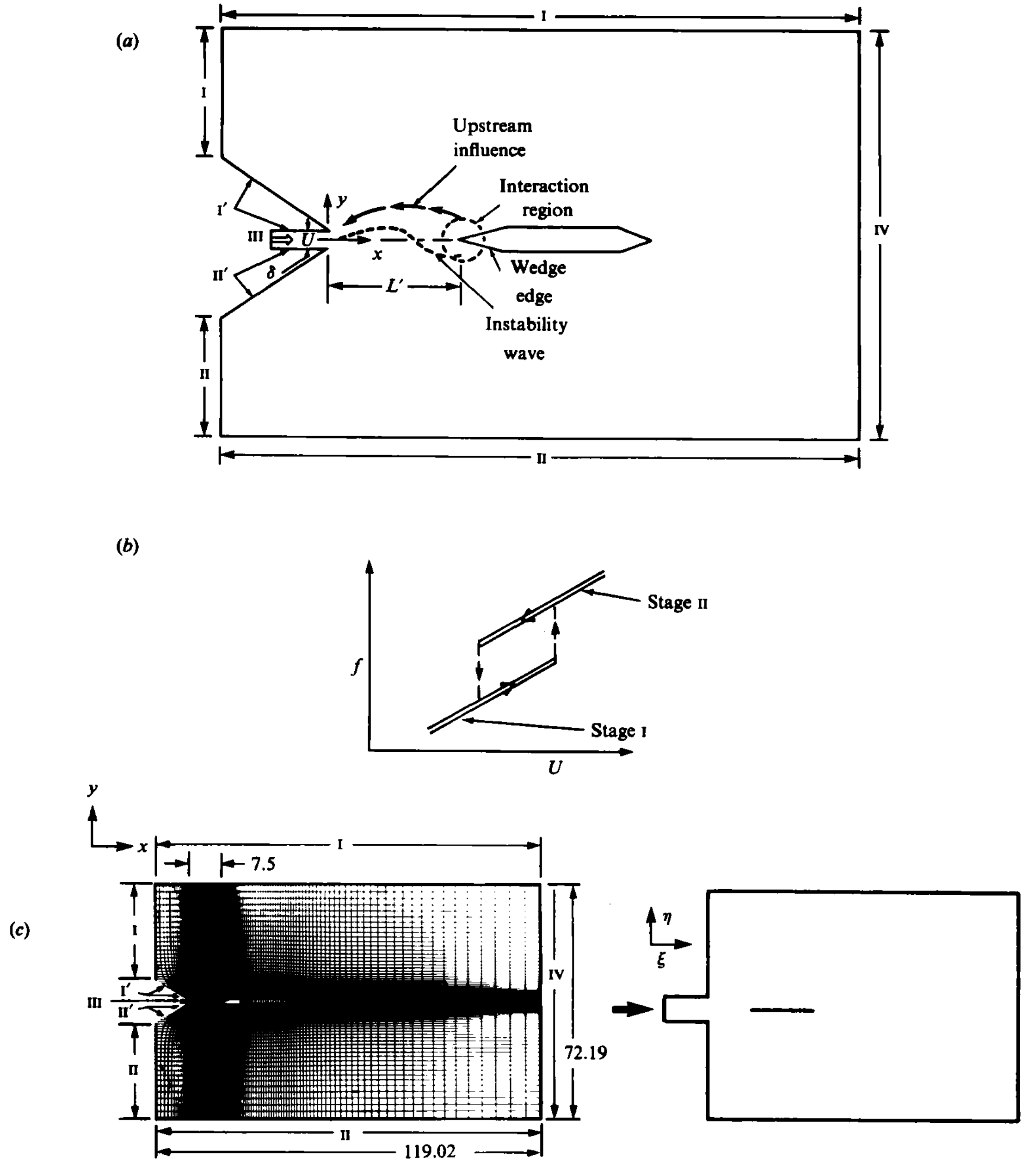

FIGURE 1. (*a*) Schematic drawing of basic features of jet-edge oscillation. (*b*) Frequency jumps, hysteresis, and definition of stages I and II. (*c*) Numerical coordinate transformation.

out to date is that the oscillating jet possesses a single predominant frequency of oscillation. Although one might detect only a single predominant frequency in the region well away from the edge (e.g. Powell 1961), a nonlinear oscillating jet actually shows the existence of multiple frequencies and their interactions (Lucas & Rockwell 1984; hereinafter referred to as LR). The numerical results of the present paper verify this multiplicity of frequencies. Energy exchange between multiple frequency components must influence the amplitude of the predominant component of the jet, the distribution of the pressure field on the wedge, and the surrounding sound field. In LR, a more general criterion was cited in characterizing these frequency jumps and hysteresis effects: a sudden increase in the number of multiple frequencies corresponds to a jump to a higher stage of oscillation and vice versa. The numerical results of this paper suggest this criterion is a valid one.

Numerical results are obtained for the following aspects of the jet-edge flow: (*i*) the spectral evolution of the jet from separation to impingement, (*ii*) detailed mechanics of vortex interaction at the edge, (*iii*) consequence of the feedback that modulates the sensitive region of the jet shear layers near separation, (*iv*) frequency jumps and hysteresis effects and (*v*) spectral analysis of numerically calculated wedge pressures and wedge torque and lift. Preliminary numerical results were presented in Ohring (1983).

2. Mathematical formulation

A numerical transformation is used that maps boundary-fitted coordinates (the boundaries being coordinate lines) in physical space onto a Cartesian coordinate system of a computational space. Poisson equations are used to generate the coordinates. These numerical mappings have become quite commonplace for the solution of fluid-flow problems (Thompson *et al.* 1975; Thompson, Warsi & Mastin 1982). Figure 1(*c*) shows the numerical mapping of the physical-space-coordinate system on the left onto the Cartesian-coordinate system of the computational space on the right. (A Cartesian mesh (not shown) overlays the computational space.) The physical domain represented in figure 1(*c*) and schematically in figure 1(*a*) is geometrically identical, for the channel–wedge configuration, with the apparatus at Lehigh University, Bethlehem, Pennsylvania (LR) used for conducting physical experiments for the jet–edge problem under consideration. The physical domain is symmetrical about the channel centreline. The coordinate origin is at the centre of the channel nozzle. Non-dimensional lengths and heights are shown in figure 1(*c*) and are scaled by the width of the channel. The non-dimensional length L $(= L'/\delta$, figure 1*a*) of the distance from the nozzle opening to the wedge tip is 7.5. Physical-space boundaries map onto computational-space boundaries. The wedge-shaped body maps onto the slit in computational space. Geometrical corner points are excluded from the grid under the mapping. The total number of grid points is 39481.

A vorticity (ω)–stream-function (ψ) formulation of the Navier–Stokes equations is employed so that the velocity field is automatically divergence-free. The vorticity-transport equation and the Poisson equation for the stream function ψ are written in computational-space coordinates (where the computation will be performed) as

$$\omega_t = \left[\psi_\eta \omega_\xi - \psi_\xi \omega_\eta + \frac{\alpha\omega_{\xi\xi} - 2\beta\omega_{\xi\eta} + \gamma\omega_{\eta\eta} + \sigma\omega_\eta + \tau\omega_\xi}{Re\, J}\right] J^{-1}, \tag{1}$$

$$\alpha\psi_{\xi\xi} - 2\beta\psi_{\xi\eta} + \gamma\psi_{\eta\eta} + \sigma\psi_\eta + \tau\psi_\xi = J^2\omega, \tag{2}$$

where
$$\alpha = x_\eta^2 + y_\eta^2, \quad \beta = x_\xi x_\eta + y_\xi y_\eta, \quad \gamma = x_\xi^2 + y_\xi^2, \quad J = x_\xi y_\eta - x_\eta y_\xi \tag{3}$$

with
$$\sigma = J^2 Q, \quad \tau = J^2 P, \quad P(\xi) = \left[\frac{-x_{\xi\xi}}{(x_\xi)^3}\right]_B, \quad Q(\eta) = \left[\frac{-y_{\eta\eta}}{(y_\eta)^3}\right]_B. \tag{4}$$

J is the Jacobian of the transformation. Derivatives for P and Q are evaluated at the outer boundaries B to produce orthogonal grids at the outer boundaries of the physical space and to retain, as much as possible, outer-boundary gridpoint spacing in the interior (Plant 1977).

With all velocities and lengths being scaled by U (the average velocity of the Couette flow in the channel) and δ (the width of the channel), respectively, the following non-dimensionalization has been used:

$$\omega' = \left(\frac{U}{\delta}\right)\omega; \quad \psi' = \delta U\psi; \quad t' = \left(\frac{\delta}{U}\right)t; \quad p' = \rho U^2 p; \quad Re = \frac{U\delta}{\nu}; \quad St = \frac{f\delta}{U}. \tag{5}$$

In the above, primed quantities are dimensional. The constants, ρ, ν are, respectively, the density and kinematic viscosity. Time and pressure are, respectively, t and p. The non-dimensional parameters Re and St are, respectively, the Reynolds number and Strouhal number (non-dimensional frequency), with f a dimensional frequency.

From the analytic solution for Couette flow in a channel (Schlichting 1979) it is easily shown (using the present scaling) that

$$\frac{\mathrm{d}p}{\mathrm{d}x} = -\frac{12}{Re}, \tag{6}$$

where $\mathrm{d}p/\mathrm{d}x$ is the non-dimensional constant pressure gradient for the Couette flow. Based on (6), the following boundary conditions are employed (refer to figures 1*a* and *c*): $\psi = -\frac{1}{2}$, $\omega = 0$ at boundary I; $\psi = -\frac{1}{2}$, $\psi_\mathrm{n} = 0$ (no slip) at I′; $\psi = \frac{1}{2}$, $\omega = 0$ at II; $\psi = \frac{1}{2}$, $\psi_\mathrm{n} = 0$ (no slip) at II′; $\psi = -\frac{3}{2}y - 2y^3$, $\omega = 12y$ (Couette flow) at III; and $\psi = \psi_\mathrm{b}(t)$, $\psi_\mathrm{n} = 0$ (no slip) at the wedge-shaped body. (The subscript n refers to the normal derivative at the boundary.) Note that portions of I′ and II′ are, respectively, the upper ($y = \frac{1}{2}$) and lower ($y = -\frac{1}{2}$) channel walls. The function $\psi_\mathrm{b}(t)$ is part of the solution and must be computed. Convective outflow conditions for ω and ψ_ξ with convection by the local horizontal velocity (Mehta & Lavan 1975) are used at IV.

All boundaries are walls except III and IV (the inflow and outflow boundaries, respectively). The condition $\omega = 0$ at a wall is equivalent to imposing perfect slip (Lugt & Ohring 1975). The large distance of the outer walls from the jet, in combination with this boundary condition, results in the jet being unaffected by the outer walls. The no-slip condition is applied at the near walls by computing the vorticity on those walls taking the no-slip condition into account. The value $\psi_\mathrm{b}(t)$ at a time instant is computed using a procedure given in Sood & Elrod (1974) to keep the pressure single-valued in the flow field.

The initial-boundary-value problem is completed with the initial conditions of Couette flow in the channel, potential flow elsewhere and vorticity sheets at no-slip walls I′, II′ and at the wedge-shaped body surface.

Fluid pressure at the wedge, and also fluid-exerted torque and lift due to pressure at the wedge, have been computed. By taking a suitable linear combination of the Navier–Stokes equations expressed in computational-space coordinates one obtains, after non-dimensionalization,

$$p_0 - p(\xi) = \int_{\xi=\xi_0}^{\xi} \left\{ -\frac{\beta\omega_\xi - \gamma\omega_\eta}{Re\,J} + x_\xi u_t + y_\xi v_t + \tfrac{1}{2}(u^2+v^2)_\xi - x_\xi v\omega + y_\xi \omega u \right\} \mathrm{d}\xi'. \tag{7}$$

The reference pressure p_0 is arbitrarily set to zero at the centre of the upstream end of the channel (boundary III in figures 1*a* and *c*).

Equation (7) is first used to determine the pressure at the grid point on the lower side of the wedge nearest the tip. This is done by integrating (7), in computational space, along the centreline from the upstream end of the channel (where $p = p_0 = 0$)

to the first grid point on the lower side of the slit. The pressure is then determined on the remainder of the body by integrating (7) around the body surface. For this part of the pressure computation the last five terms of the integrand are zero owing to the no-slip condition on the body. Single-valuedness of the pressure is assured by the solution process for $\psi_b(t)$. The pressure at the wedge is negative most of the time because of (6) and the choice of p_0.

Torque about the wedge tip and lift due to fluid pressure have been computed only at the surfaces of the wedge itself and not the afterbody. (Frictional forces contribute nothing to the total torque exerted on the wedge and are a negligible part of the fluid-exerted lift.) The total moment CM_p and lift CL_p per unit breadth due to fluid pressure are given by

$$CM_p = \int_{(i)} ps \,\mathrm{d}s - \int_{(ii)} ps \,\mathrm{d}s, \tag{8}$$

$$CL_p = \int_{(i)} p\cos\beta \,\mathrm{d}s - \int_{(ii)} p\cos\beta \,\mathrm{d}s. \tag{9}$$

Here, (i) and (ii) refer, respectively, to the lower and upper wedge surfaces: s is the wedge surface arclength measured from the wedge tip and $\beta = \frac{1}{12}\pi$, half the included wedge angle. In computational-space coordinates

$$CM_p = \left(\int_{(i)} - \int_{(ii)}\right) \frac{p(x-x_w)\,x_\xi \,\mathrm{d}\xi}{\cos^2\beta}, \tag{10}$$

$$CL_p = \left(\int_{(i)} - \int_{(ii)}\right) p x_\xi \,\mathrm{d}\xi, \tag{11}$$

$$CM_p = d\,CL_p, \tag{12}$$

where x_w is the x-coordinate of the wedge tip, d is the fulcrum distance and use is made of the fact that $\mathrm{d}x = x_\xi \,\mathrm{d}\xi$ at the wedge since $\mathrm{d}\eta = 0$. The dimensional counterparts of CM_p and CL_p have been scaled, respectively, by $\rho U^2\delta^2$ and $\rho U^2\delta$.

3. Numerical method

Second-order finite differences replace derivatives throughout. An implicit, second-order (in time and space) Crank–Nicholson finite-difference procedure was used to advance the solution in time. At each time step several iterations were necessary to satisfy all the following convergence criteria. The percentage change from iterate to iterate in ψ_b and wall-generated vorticity (at all no-slip walls) had to be less than 1 % with these convergence tests not applying if $\psi_b < 0.001$ or $\omega_{\text{wall}} < 0.05$. In addition, the global L_2 error norm for ω from (1) and for ψ from (2) each had to be less than 0.001 for convergence.

Each iteration consisted of a sweep of (1) followed by a sweep of (2) using a four-colour overrelaxation scheme for each sweep with an overrelaxation factor of 1.6. These iterations were fully vectorized on the Cray 1-S upon which the numerical computation was performed.

A device that proved useful was to obtain initial guesses for ψ and ω at a new time step by extrapolation from several previous time steps. A time step of 0.008 was used except for $Re = 650$, for which a time step of 0.006 was used. Much smaller time steps are used for all the cases near the sensitive time region of $t = 0$.

In this paper Fourier analysis has been performed on discrete numerical data obtained from the numerical flow solutions by using the discrete Fourier transform.

Let $\{g_r\}$, $r = 0, 1, 2, \ldots, (N-1)$, be a series of discrete functional values of a function g equally spaced in time t such that $T = N\Delta$, where T is the period, N is the number of equally spaced time intervals of the period, and Δ is the time interval. The discrete Fourier transform (Newland 1975, p. 116) of the series $\{g_r\}$, $r = 0, 1, 2, \ldots, (N-1)$, is given by

$$\tilde{G}_k = \frac{1}{N}\sum_{r=0}^{N-1} g_r \, e^{-i(2\pi kr/N)}, \quad k = 0, 1, 2, \ldots, (N-1). \tag{13}$$

Here $\tilde{G}_k$ in (13) is an approximation for

$$G_k = a_k - ib_k = \frac{1}{T}\int_0^T g(t)\, e^{-i(2\pi kt/T)}\, dt, \tag{14}$$

where a_k and b_k are the Fourier coefficients of the Fourier series for the continuous, periodic function $g(t)$ with period T. Of particular interest is

$$A_{\tilde{G}_k} = |\tilde{G}_k|, \quad k = 0, 1, 2, \ldots, (N-1). \tag{15}$$

Notationally, the aggregate of amplitudes $\{A_{\tilde{G}_k}\}$, $k = 0, 1, 2, \ldots, (N-1)$ will be referred to as $A_{\tilde{G}}$ in the text.

A number of checks, procedures, and observations were employed to ensure reliability in the use of the discrete Fourier transform (13) and are outlined below.

To obtain confidence that the maximum frequency that can be detected from data sampled at time spacing Δ (the so called Nyquist frequency $1/(2\Delta)$) was greater than any other frequency inherent in the time series and thus prevent aliasing (Newland 1975, p. 120), $4N$ points (obtained by linear interpolation) as well as N points, for the period T were used as a check in the Fourier analysis of the time histories. Results showed no change of any significance in Fourier amplitude values.

Care has been taken to choose in all cases $T = nt_{\frac{1}{3}\beta}$, n an integer, where $t_{\frac{1}{3}\beta}$ is the period of the dominant frequency $\frac{1}{3}\beta$.

It was observed in all cases that $|\tilde{G}_k| \rightarrow 0$ as $k \rightarrow \frac{1}{2}N$ $(k = 0, 1, \ldots, \frac{1}{2}N)$ well before $k = \frac{1}{2}N$. Usually $|\tilde{G}_k|$ was essentially zero beyond $k = \frac{1}{6}N$.

The Fourier analysis has been applied directly to the numerical data from the numerical flow solution. No filtering of the numerical data has been used. Filtering of the numerical data is not justified because only a few cycles are used in the Fourier analysis owing to the present expense of flow computation. Experimentally, by contrast, tens of cycles of a continuous signal can be used in the Fourier analysis.

For the Reynolds number equal to 650 case, $\Delta = 0.3$. For all other Reynolds-number cases in this paper, $\Delta = 0.4$. Values for T, N, and n will be given in §4.

4. Numerical results

Four Reynolds-number cases were considered in the present numerical study:

(*i*) $Re = 250$ (from $t = 0$ to $t = 87.39$).

(*ii*) $Re = 650$ (from $t = 87.39$ to $t = 132.39$). This case was abruptly started from the numerical solution for $Re = 250$ at $t = 87.39$.

(*iii*) $Re = 450$ (from $t = 132.39$ to $t = 212.39$). This case was abruptly started from the numerical solution for $Re = 650$ at $t = 132.39$ and will be denoted $Re = 450$ (from 650).

(*iv*) $Re = 450$ (from $t = 87.39$ to $t = 167.39$). This case was abruptly started from the numerical solution for $Re = 250$ at $t = 87.39$ and will be denoted $Re = 450$ (from 250).

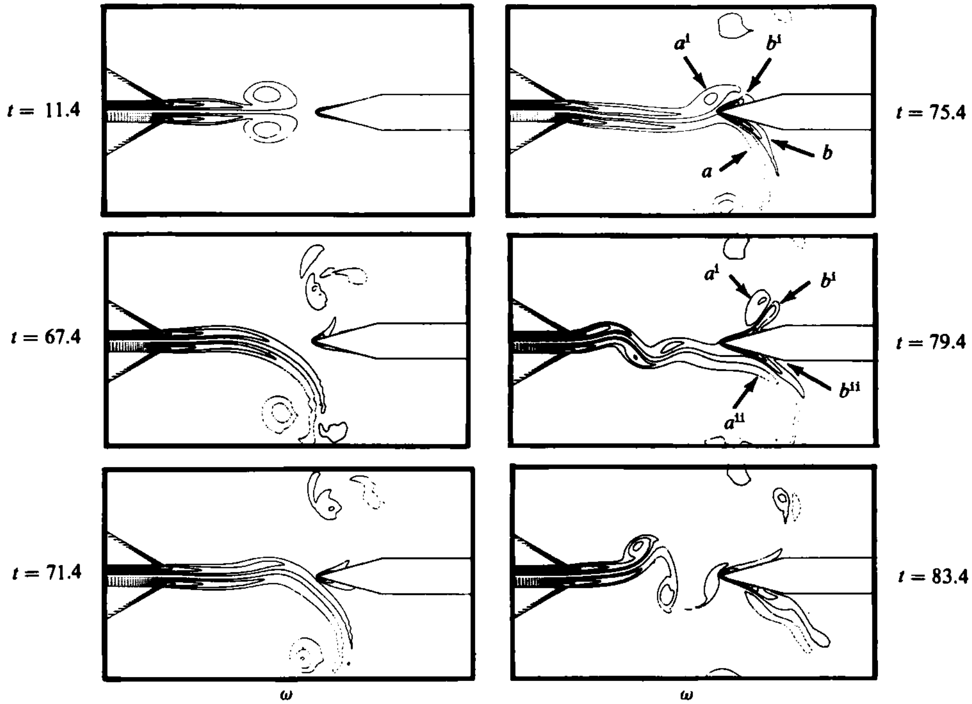

FIGURE 2. Contour plots for $Re = 250$ at selected times.

4.1. *Flow visualizations*

Figure 2 shows computer-drawn equivorticity lines at selected times for the numerical solution for $Re = 250$. (In the flow contour plots throughout this paper, equivorticity-line values are $\pm 1, \pm 2, \dots$ and streamline values are $\dots -0.2, -0.1, 0, 0.1, 0.2 \dots$. Negative equivorticity lines are dashed; positive ones are solid. However, in regions of high grid-point density, the dashed lines will appear solid.) At $t = 0$, due to the initial conditions, the jet flow separates at the corners of the channel nozzle, resulting in starting vortices which are then convected downstream. (In this paper, vortices shed from the jet shear layers and the wedge are defined as regions of vorticity with a local extremum.) This is seen at $t = 11.4$. The effect of the starting vortices is very similar to the cast-off vortex from the trailing edge of a wing abruptly started from rest (Goldstein 1938). The flow is still symmetric at $t = 11.4$. In nature the jet is unstable and therefore an asymmetric disturbance is abruptly introduced into the numerical scheme at $t = 11.4$. The disturbance consists of applying a 'moving belt' condition in the lower channel wall for 0.8 non-dimensional time units followed by application of the same condition in the upper channel wall for 0.8 time units.

Because of lingering transient effects from the asymmetric disturbance and limited availability of computer time, a cycle for $Re = 250$ completely free of start-up transients was not obtained. (In the laboratory many cycles are required before periodic quasi-steady-state cycles free of start-up disturbances can be obtained for $Re = 250$, Rockwell, private communication.) However, the pictures from $t = 67.4$ through $t = 83.4$ do show a cycle characterized by a complete jet oscillation. The pictures from $t = 67.4$ through $t = 75.4$ clearly show half a complete jet oscillation. The jet is below the wedge at $t = 67.4$ and the jet vortex a will induce a vortex of opposite sign b on the lower side of the wedge due to viscosity (as seen at $t = 75.4$). The jet rises with the jet vortex a^{i} inducing a vortex of opposite sign b^{i} at the upper side of the wedge ($t = 75.4$). At $t = 79.4$, the jet drops below the wedge with vortex a^{ii} inducing vortex b^{ii} on the lower side of the wedge. The jet oscillation should be completed at $t = 83.4$ but transient effects interfere. However, the numerical results do show a long jet stem, the dominant feature for $Re = 250$ as seen in the laboratory, and the jet oscillating with a single predominant frequency which is designated as $\frac{1}{3}\beta$. This designation expresses the relationship of this frequency to another fundamental frequency, β, which will shortly be discussed. At a particular side of the wedge, counter-rotating vortex pairs are formed at this same frequency $\frac{1}{3}\beta$ (i.e. a, b and a^{ii}, b^{ii} pairs at lower wedge side) leading to an upstream disturbance that modulates the sensitive region of the shear layer near the channel nozzle at frenquency $\frac{1}{3}\beta$. LR refers to a jet oscillating with a single predominant frequency as a stage I oscillation (figure 1*b*). Such an oscillation occurs at low values of Reynolds number.

Figure 3 shows computer-drawn equivorticity lines at equal time intervals for the numerical solution for the case $Re = 650$ representing a jump to stage II oscillations from the stage I situation of $Re = 250$. Streamlines are also shown for comparison with the equivorticity lines.

At $t = 102.4$ is shown a large-scale vortex a (newly formed from the lower jet shear layer near $t = 99.4$) and two associated jet-shear-layer vortices a^{i} and b^{i}. The vortex pair a^{i}, b^{i} is counter-rotating, i.e. a^{i} and b^{i} are of opposite sign, which slides underneath vortex a at impingement ($t = 105.4$) with part of the vortex pair a^{i}, b^{i} intercepted by the wedge. Meanwhile, the large-scale vortex a^{ii} (newly evolved from the upper jet shear layer at $t = 102.4$) and two associated jet-shear-layer vortices a^{iii} and b^{iii} of opposite sign, forming the counter-rotating vortex pair a^{iii}, b^{iii}, are visible at $t = 108.4$. The vortices a^{iii} and b^{iii} slide beneath vortex a^{ii} at impingement with part of the counter-rotating vortex pair a^{iii}, b^{iii} intercepted at the wedge at $t = 114.4$. The process just described, from approximately $t = 99.4$ to $t = 117.4$, constitutes one complete jet oscillation cycle or flapping up and down of the jet. The cycle repeats, with vortices a^{iv}, a^{v}, and b^{v}, from $t = 117.4$ on. Note that the vortices a^{iii} and b^{iii} rotate about the large vortex a^{ii} from $t = 114.4$ to $t = 120.4$. (A similar process occurs at $t = 120.4$ and $t = 123.4$ involving vortices a^{iv} and a^{v}, b^{v} and to a lesser extent for vortices a, a^{i}, b^{i} at $t = 105.4$ and $t = 108.4$ due to diffusion.)

The complete time period of the jet oscillation cycle is $t_{\frac{1}{3}\beta}$ corresponding to the rate of formation of large-scale vortices a, a^{ii} (i.e. the time period from $t = 102.4$ to 111.4 is one half cycle, the other half cycle is from $t = 111.4$ to 120.4). Large-scale vortex a^{iv} at $t = 120.4$ represents the start of the repetition of the cycle. During the complete jet oscillation cycle negative sign (clockwise rotating) vortices a, a^{i}, b^{iii} are generated in the lower jet shear layer and positive sign (counterclockwise rotating) vortices a^{ii}, a^{iii}, b^{i} are generated in the upper jet shear layer. The a, a^{ii} vortices correspond to every third jet shear-layer vortex. Thus, each incident jet shear-layer vortex is generated at frequency β. It will be shown from Fourier analysis that the upstream influence of the set (of large vortices a, a^{ii}) which occurs at frequency $\frac{1}{3}\beta$ dominates the region of the jet near separation at the nozzle. Since each incident shear-layer vortex interacts with the wedge, substantial upstream influence at frequency β also occurs as shown from Fourier analysis later in this paper. The frequency $\frac{2}{3}\beta$, corresponding to one-half of a jet oscillation cycle, will be shown later in the paper to be one of the dominant frequencies for the wedge pressure, torque and lift.

The time $t_{\frac{1}{3}\beta}$ for a complete oscillation cycle for $Re = 650$ (from visual inspection of figure 3) is 18 time units. (Fourier analysis will show it to be approximately 17.7

time units). The time $t_{\frac{1}{3}\beta}$ for an oscillation cycle for $Re = 250$ (from visual inspection of figure 2) is approximately 16 time units, which is roughly the same as $t_{\frac{1}{3}\beta}$ for $Re = 650$. Therefore, to summarize, the low-frequency component $\frac{1}{3}\beta$, which is the most unstable frequency of the stage I oscillation ($Re = 250$; figure 2), exists in stage II ($Re = 650$; figure 3) also, owing to a remarkable readjustment of the vortex–edge interaction patterns with increasing Reynolds number. The $\frac{1}{3}\beta$ component is associated with large-scale vortex formation at the edge; in stage I, these vortices arise from shear-layer instability at $\frac{1}{3}\beta$, while in stage II they result from growth and interaction of the incident vortices of the unstable jet shear layer at frequency β, giving rise to the vortex patterns of figure 3 which are in good agreement with vortex patterns obtained experimentally for $Re = 600$ (LR; Kaykayoglu & Rockwell).

Later in the paper it will be shown for $Re = 450$ (from 650) and $Re = 450$ (from 250) that $t_{\frac{1}{3}\beta}$ is approximately 17.1 and 17.9, respectively. Thus, for the Reynolds-number cases considered in this paper from $Re = 250$–650, the Strouhal number St associated with the frequency $\frac{1}{3}\beta$ is approximately 0.06. LR found $St = 0.04$ for a range of $Re = 250$–1300. Their physical experiments used a breadth-to-width ratio of 48 for the nozzle.

Experimentally it has been found that different channel span-to-width aspect ratios and different channel-span end conditions (whether open or closed) can produce changes of 20–25 % in the value of St. However, the core flow is two-dimensional along the span (Rockwell, private communication). Numerically, in this paper, the nozzle breadth-to-width ratio is infinite. This and other subtle differences between the numerical and experimental method and their respective global geometries could easily account for this discrepancy for St. The important thing here is that both methods agree on their description of the dominant frequencies β and $\frac{1}{3}\beta$ and the resultant flow processes.

The motivation for considering the cases $Re = 450$ (from 650) and $Re = 450$ (from 250) was based on the concept of frequency jumps and hysteresis effects in jet–edge systems which was first considered by Powell (1961) and has subsequently received considerable attention, as summarized by Rockwell (1983). Although efforts had largely focused on the variation of a single predominant frequency component in characterizing these jumps and hysteresis effects (see figure 1*b* and discussion in § 1), LR proposed a more general criterion: a sudden increase in the number of frequencies (whose component amplitudes are at least 10 % of the maximum component amplitude) corresponds to a jump to a higher stage of oscillation and vice versa. They found experimentally that for increasing Re there is a sudden increase in the number of frequency components in the range $450 < Re < 550$ and that for decreasing Re, there is a sudden decrease in the number of frequency components in the range $300 < Re < 375$. These two ranges are very close to the values for which Powell observed upward and downward jumps respectively in the predominant frequency of oscillation on the basis of far-field microphone measurements and are indicated schematically by the vertical arrows in figure 1(*b*).

Therefore, one should expect the $Re = 450$ (from 650) case, where the Reynolds number is decreased, to (*i*) have flow patterns very similar to $Re = 650$ and (*ii*) to retain the number of multiple frequencies of $Re = 650$. For the case $Re = 450$ (from 250), where the Reynolds number is increased, one should expect the flow patterns to exhibit to a certain extent the flow patterns of the higher stage II ($Re = 650$) while retaining some of the aspects of the flow patterns of the lower stage I ($Re = 250$). This should be so since $Re = 450$ is right at the edge of the lower end of the Reynolds-number range where a jump occurs to a higher stage II when increasing the Reynolds number

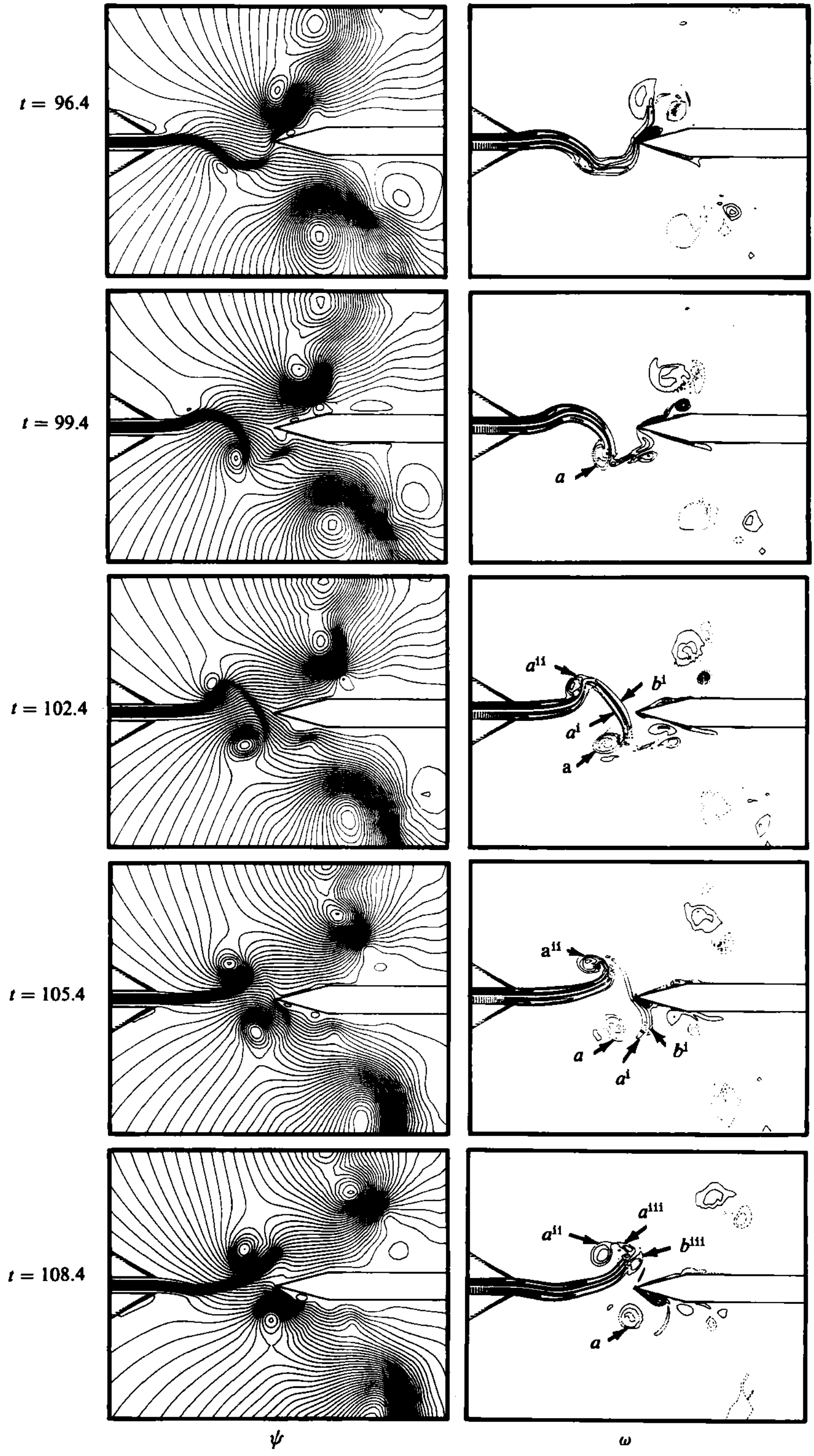

FIGURE 3. Time sequence of contour plots for $Re = 650$.

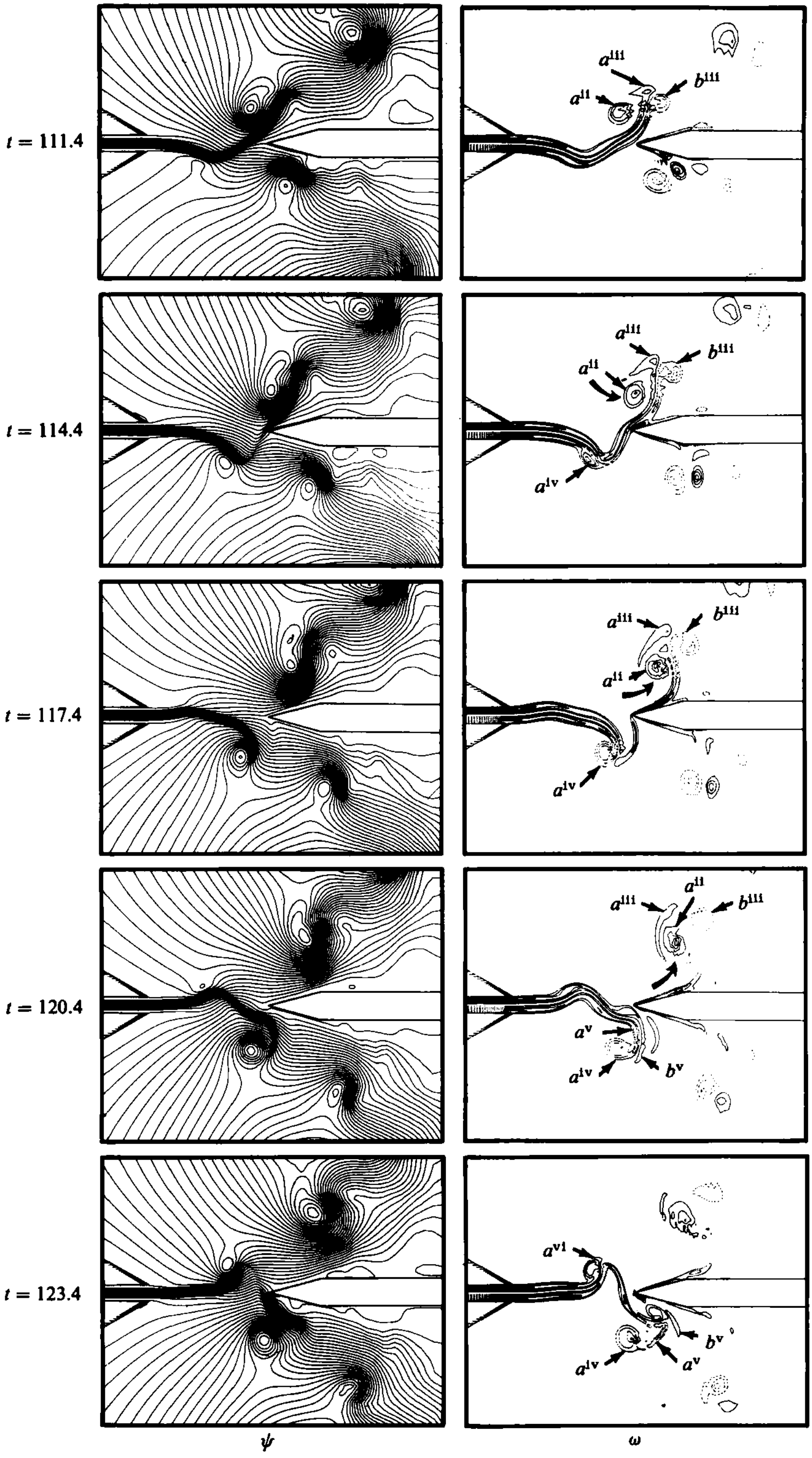

FIGURE 3 (*cont.*)

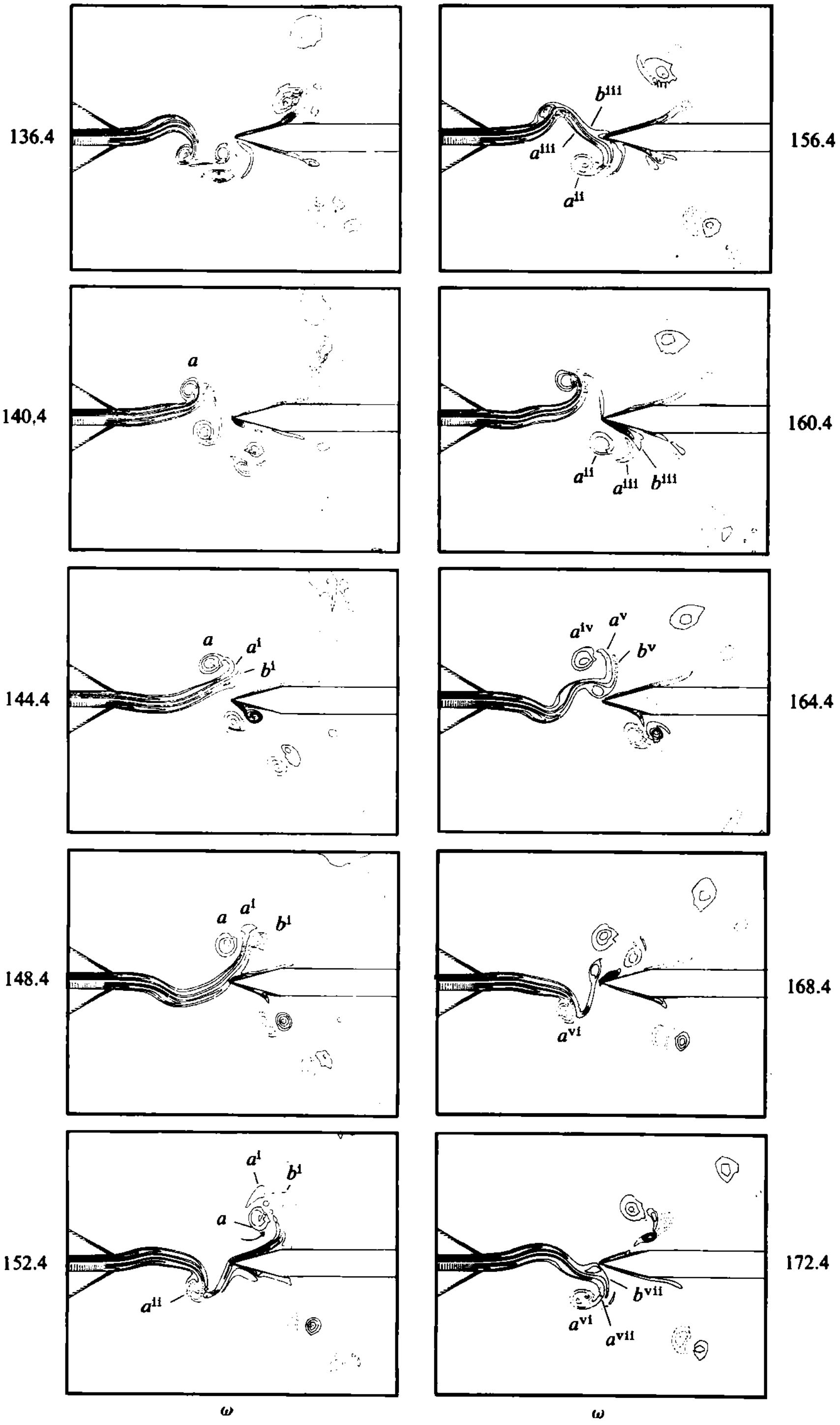

FIGURE 4. Time sequence of contour plots for $Re = 450$ (from 650).

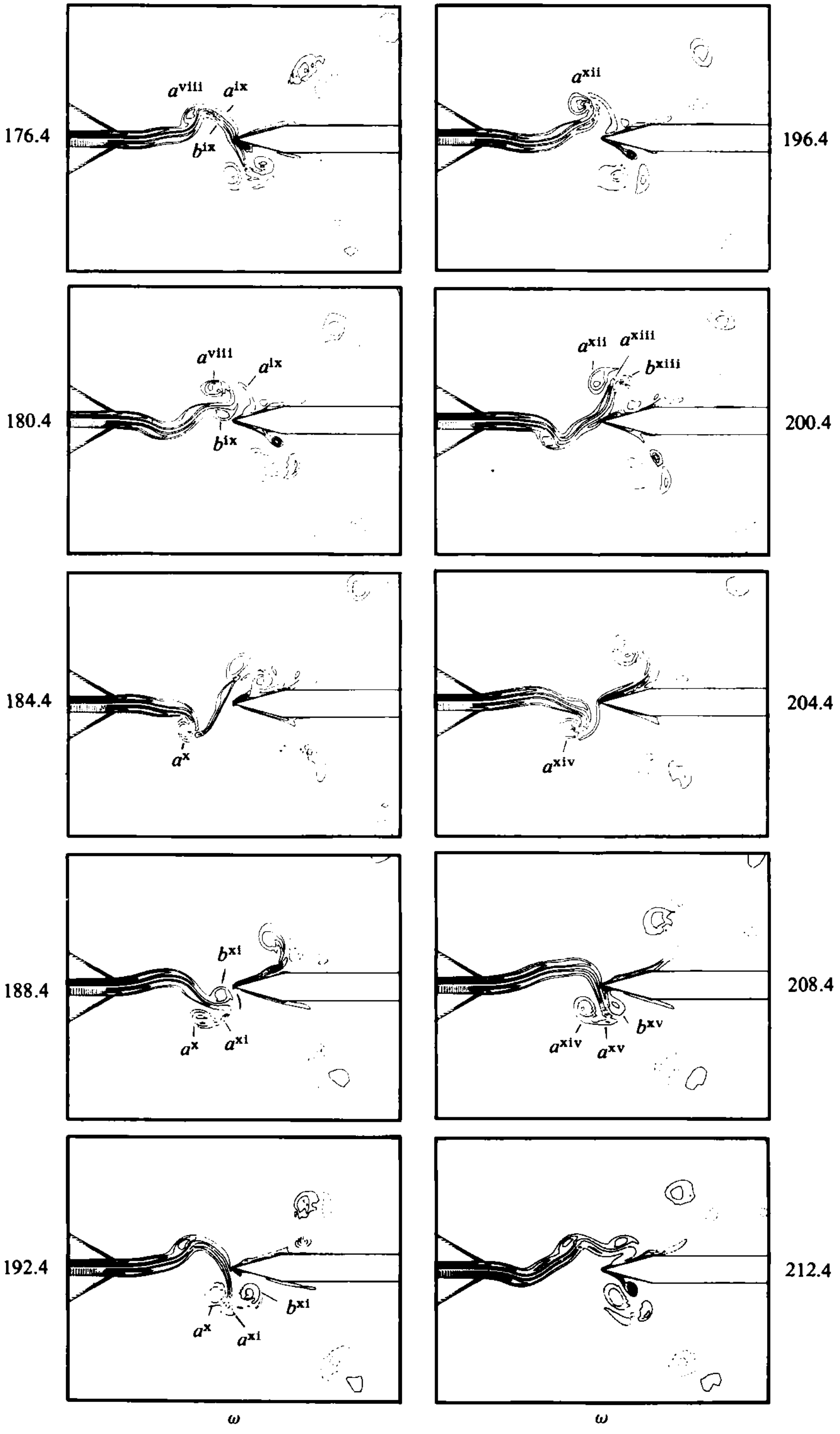

FIGURE 4 (*cont.*)

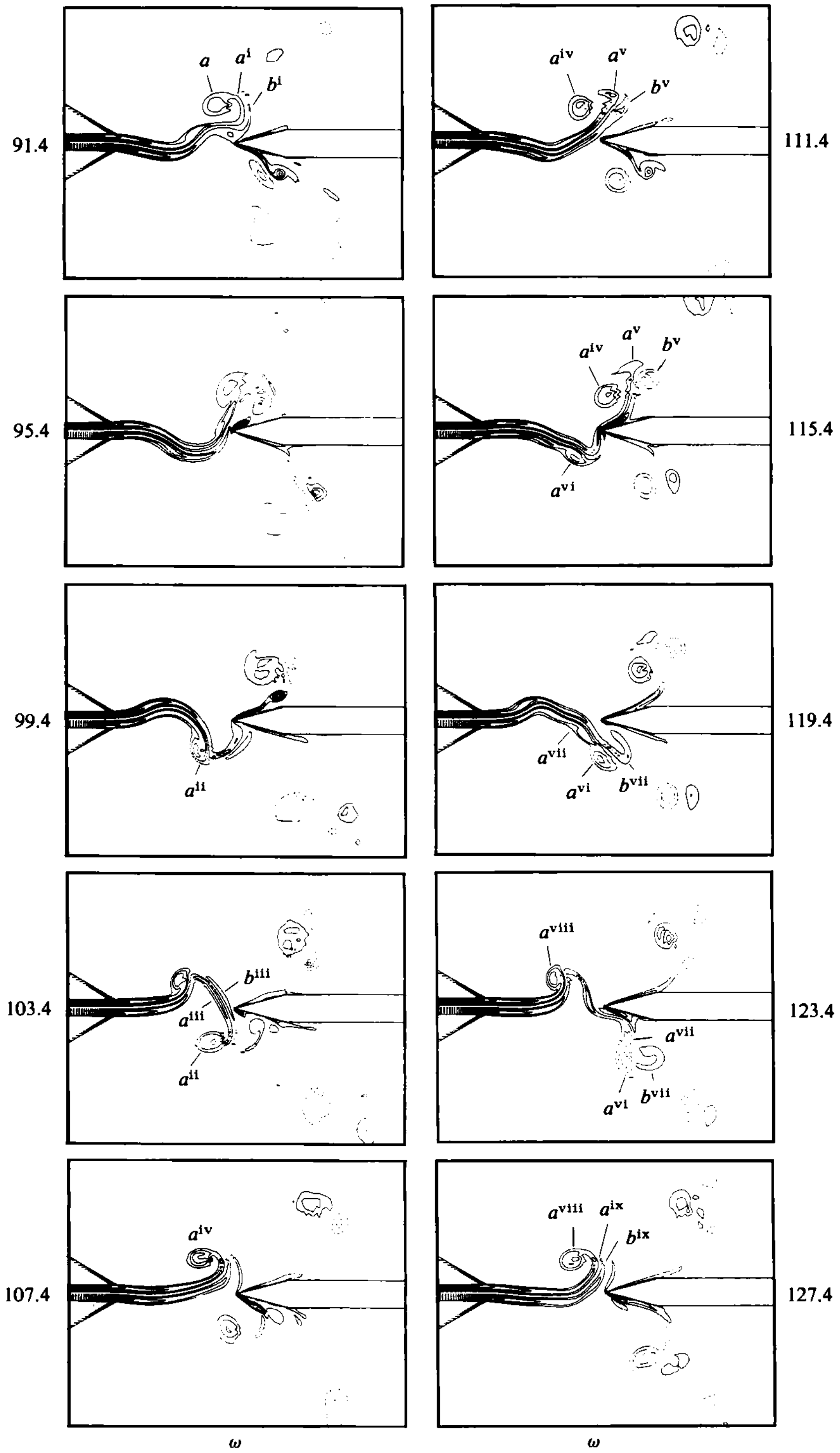

FIGURE 5. Time sequence of contour plots for $Re = 450$ (from 250).

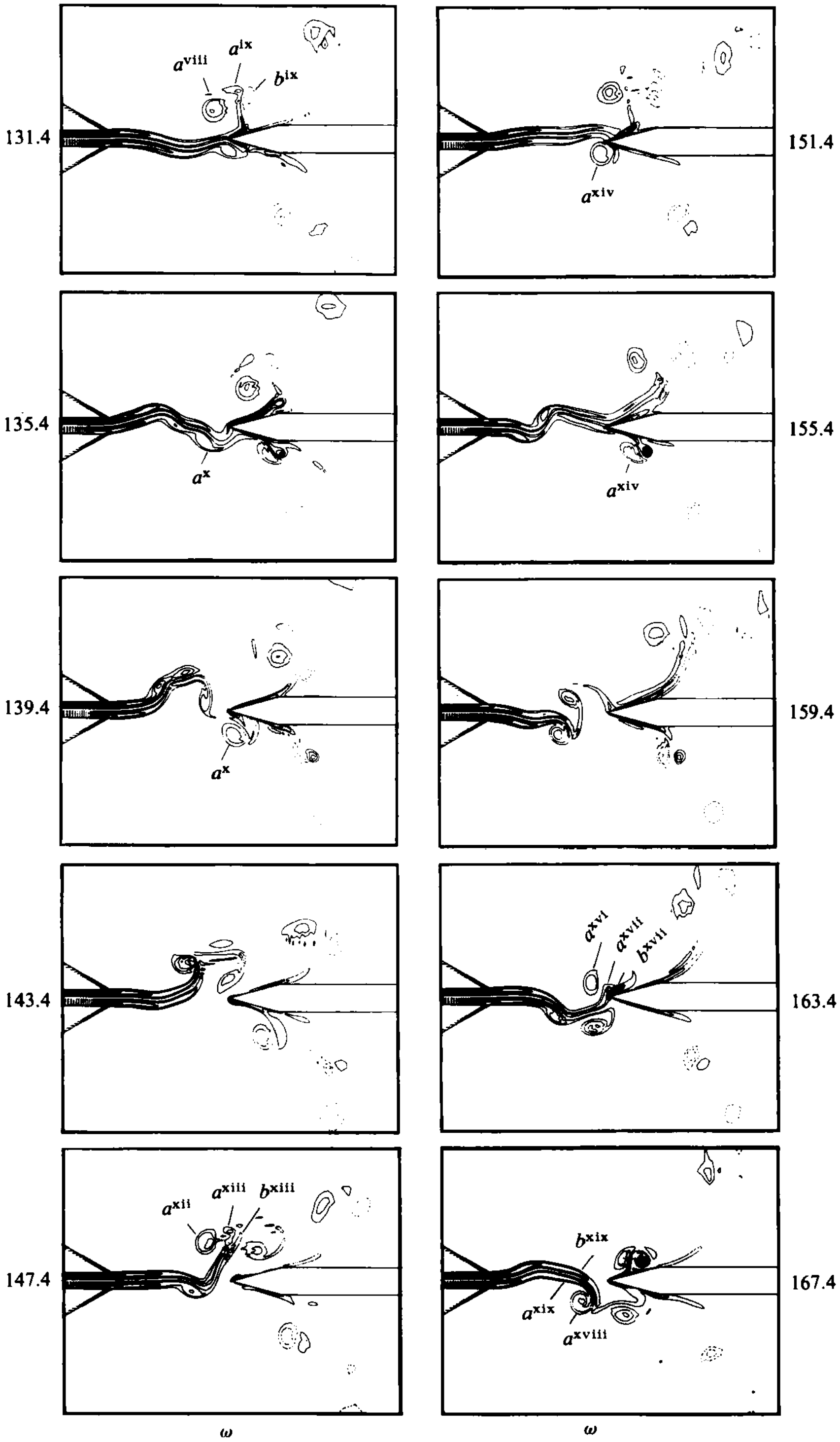

FIGURE 5 (*cont.*)

from below. A moderate increase in the number of multiple frequencies from that of $Re = 250$ is also expected for $Re = 450$ (from 250) for the reasons just given. The aforementioned expectations are borne out in the computational results, thereby displaying the concept of frequency jumps and hysteresis effects.

Figures 4 and 5 show equivorticity lines for cases $Re = 450$ (from 650) and $Re = 450$ (from 250), respectively. Note that the same notation for the vortices is used as for $Re = 650$ and that the time intervals between consecutive pictures is now 4 time units rather than 3 time units used for $Re = 650$.

For $Re = 450$ (from 650) in figure 4, the flow patterns are strikingly similar spatially and in time to those of $Re = 650$, despite an increase in diffusion effects.

For $Re = 450$ (from 250) in figure 5, the flow patterns are strikingly similar to those of $Re = 650$ from $t = 91.4$ to $t = 127.4$. However, at $t = 131.4$, one sees a long jet stem impinging on the wedge, which is the dominant feature of $Re = 250$. From $t = 135.4$ to $t = 147.4$ the flow pattern gradually assumes the characteristics of $Re = 650$ but is again interrupted at $t = 151.4$ with the characteristics of $Re = 250$, that of the long jet stem impinging on the wedge. From $t = 155.4$ to $t = 167.4$ the flow pattern again starts to resemble that of $Re = 650$. Thus, the flow patterns of $Re = 450$ (from 250) are similar to those of $Re = 650$ most of the time but, unlike $Re = 450$ (from 650), have the dominant feature of $Re = 250$ at other times, thereby indicating a partial jump to a stage II oscillation while showing some hysteresis effects.

Figure 6 shows a global view of the flow patterns for $Re = 650$ at $t = 132.4$ in the entire physical domain upon which the calculations are performed. The flow is essentially irrotational throughout the time histories of all Reynolds-number cases considered in this paper downstream of the body in figure 6.

4.2. *Numerical spectral results along the jet*

Figure 7 shows transverse velocity (v velocity component) time histories for $Re = 250$, $Re = 650$ and $Re = 450$ (from 650) and figure 8 shows transverse-velocity time histories for $Re = 250$, and $Re = 450$ (from 250). The time histories are taken at the centre of the jet ($y = 0$) for three values of x/L: $x/L = 0.06844$ (by channel mouth); $x/L = 0.56388$ (approximately halfway to wedge tip); and $x/L = 0.9787$ (by the wedge tip). L is the non-dimensional distance from the nozzle opening to the wedge tip. In this paper L is 7.5. All distances have been scaled by the width of the channel.

For $Re = 250$, $t_{\frac{1}{3}\beta}$ was obtained from visual inspection of the flow field discussed earlier. Experimentally, for $Re = 250$, it has been found that the $\frac{1}{3}\beta$ frequency dominates and grows along the entire length of the jet with a higher harmonic $\frac{2}{3}\beta$ setting in and persisting as the jet approaches the wedge tip. The velocity traces for $Re = 250$ in figures 7 and 8 show transient effects from the initial start-up of the flow.

For $Re = 650$ and $Re = 450$ (from 650) (whose traces very closely match those of $Re = 650$, thereby again displaying hysteresis effects) the velocity time histories at $x/L = 0.06844$ show dominance of the low-frequency modulation component $\frac{1}{3}\beta$ arising from upstream influence of the large-scale vortex interaction at the wedge. The period corresponding to the frequency of vortex formation β in the jet shear layer is slightly detectable at $x/L = 0.06844$ and at $x/L = 0.56388$ and 0.9787 it becomes quite pronounced. Both $\frac{1}{3}\beta$ and β are dominant frequencies which grow along the jet.

For $Re = 450$ (from 250) in figure 8, the velocity traces are similar to those of $Re = 650$ and $Re = 450$ (from 650) except the β component is diminished at all three locations along the jet shear layer. This is in agreement with the flow visualization and discussion earlier for $Re = 450$ (from 250) since this case is at the edge of the Re range for a jump to a stage II oscillation from a stage I oscillation. The traces reveal

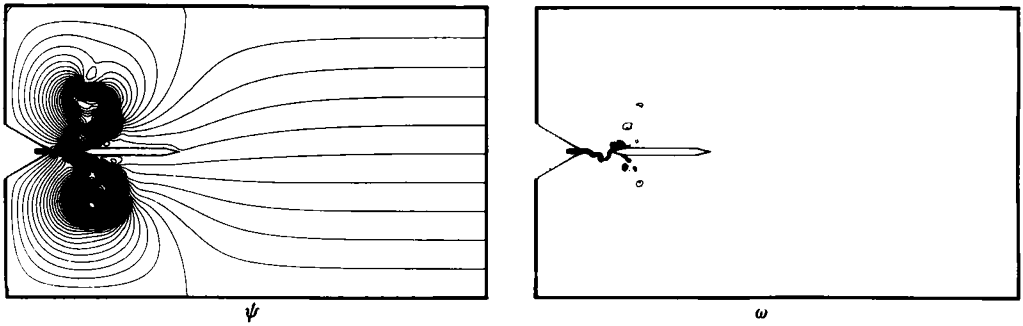

FIGURE 6. Contour plots in the entire domain for $Re = 650$ at $t = 132.4$.

a stage II oscillation with some features of a stage I oscillation (where only $\frac{1}{3}\beta$ dominates along the jet) represented by the diminished β component along the jet.

Spectral analysis was performed on the velocity traces (and later in this paper on wedge pressure, torque, and lift time histories) of the four Reynolds-number cases. For $Re = 650$, $Re = 450$ (from 650), $Re = 450$ (from 250), and $Re = 250$ the values $\{T, N, n\}$ used for the spectral analysis in this paper were $\{35.4, 118, 2\}$, $\{51.2, 128, 3\}$, $\{53.6, 134, 3\}$, and $\{39.2, 98, 2\}$, respectively and the corresponding time intervals were $t \in [96.7,\ 132.1]$, $[138.8,\ 190.0]$, $[90.6,\ 144.2]$, and $[48.2,\ 87.4]$, respectively. These values and time intervals were selected on the basis of visual inspection of the flow fields and of tabulated and graphical displays of the traces. Only for $Re = 250$ is there a noticeable discrepancy between the visual inspection of the flow field and of the traces as regards $t_{\frac{1}{3}\beta}$. For $Re = 250$, visual inspection of the flow field gave $t_\beta \approx 16.0$ while that of the traces gave $t_\beta = 19.6$. This latter value was used in the Fourier analysis. The discrepancy is due to the approximate nature of a visual determination of a complete oscillation cycle for $Re = 250$.

Figure 9 shows the growth rates of the spectral components $\frac{1}{3}\beta$, $\frac{2}{3}\beta$, β, $\frac{4}{3}\beta$, $\frac{5}{3}\beta$ of the vertical velocity along x/L for $y = 0$ for the four Reynolds-number cases. In all the Re cases the $\frac{1}{3}\beta$ component has the largest amplitude for all values of x/L. In all the Re cases the amplitudes of all the components in general grow with increasing x/L. The region with values x/L very close to 1 (the wedge-tip area) is very sensitive numerically and inaccuracy may account for the mixed behaviour of the amplitudes in this region. For all Re-cases the largest amplitudes generally (for all values x/L) are those of $\frac{1}{3}\beta$ and β. The presence of these five multiple frequencies and more for all the Re-cases (except $Re = 250$) are due to the patterns of interacting vortices in the vicinity of the wedge that give rise to a multiple-frequency upstream influence; corresponding conversion of this influence to vorticity fluctuations in the sensitive region of the shear layer near separation; and amplification of these multiple frequency disturbances (amplitude growth) in the downstream-evolving shear layer. The upstream influence excites (in primarily the $\frac{1}{3}\beta$ and β components) the downstream-evolving instability wave. All the components of the instability wave may be related to sum and difference frequencies of the primary components $\frac{1}{3}\beta$ and β, i.e. $\frac{1}{3}n\beta \pm m\beta$ (n, m integral) through nonlinear interaction between the $\frac{1}{3}\beta$ and β components throughout the instability wave. The spectral character of the modulated shear layer near the nozzle exit is the same as that incident upon the edge due to nonlinear growth of the instability wave. It should be stated that, for $Re = 250$, LR found, in experiments, multiple frequency components of smaller amplitude than those depicted in figure 9. Note that the β component for $Re = 450$ (from 250) is

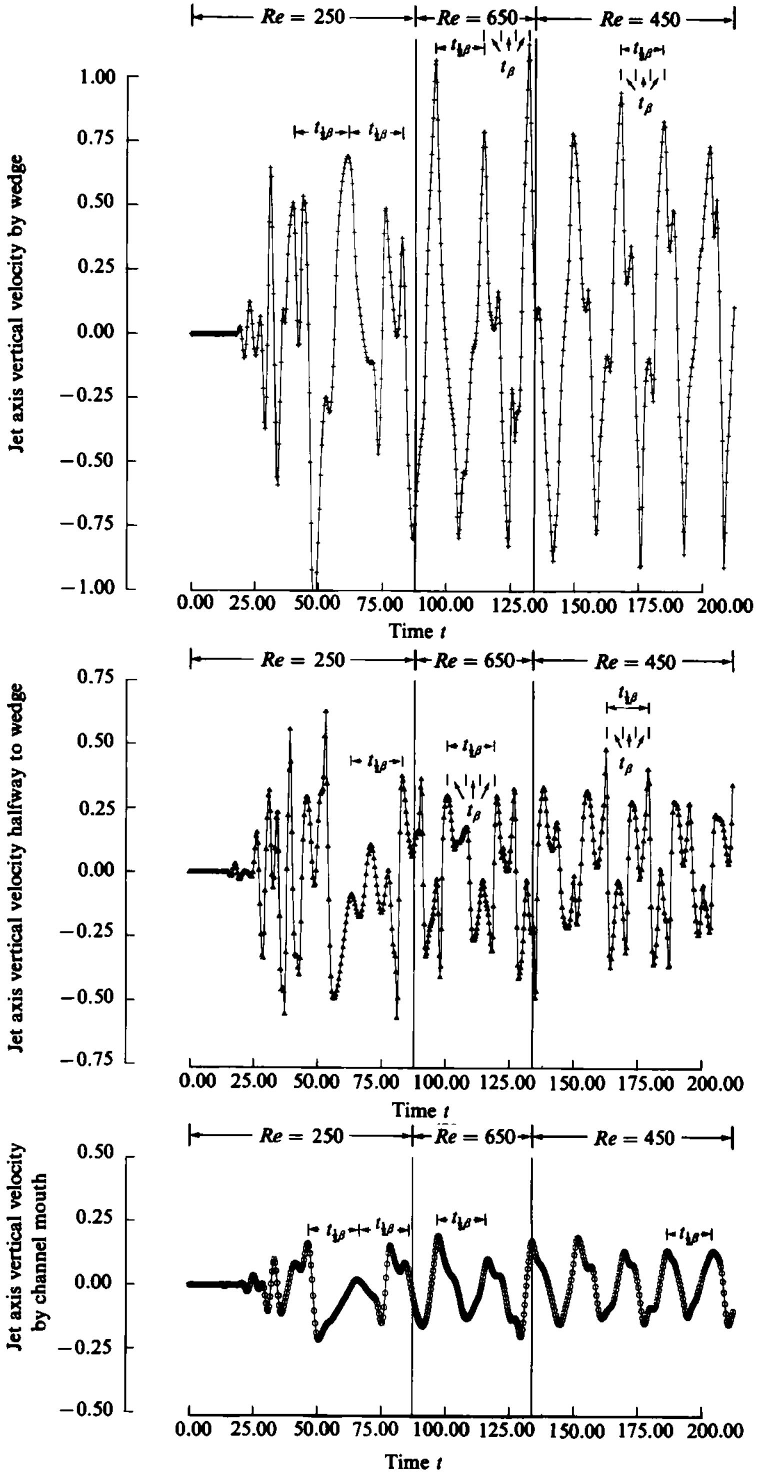

FIGURE 7. Transverse-velocity time histories at three locations along the jet centreline ($y = 0$) for $Re = 250$, $Re = 650$, and $Re = 450$ (from 650).

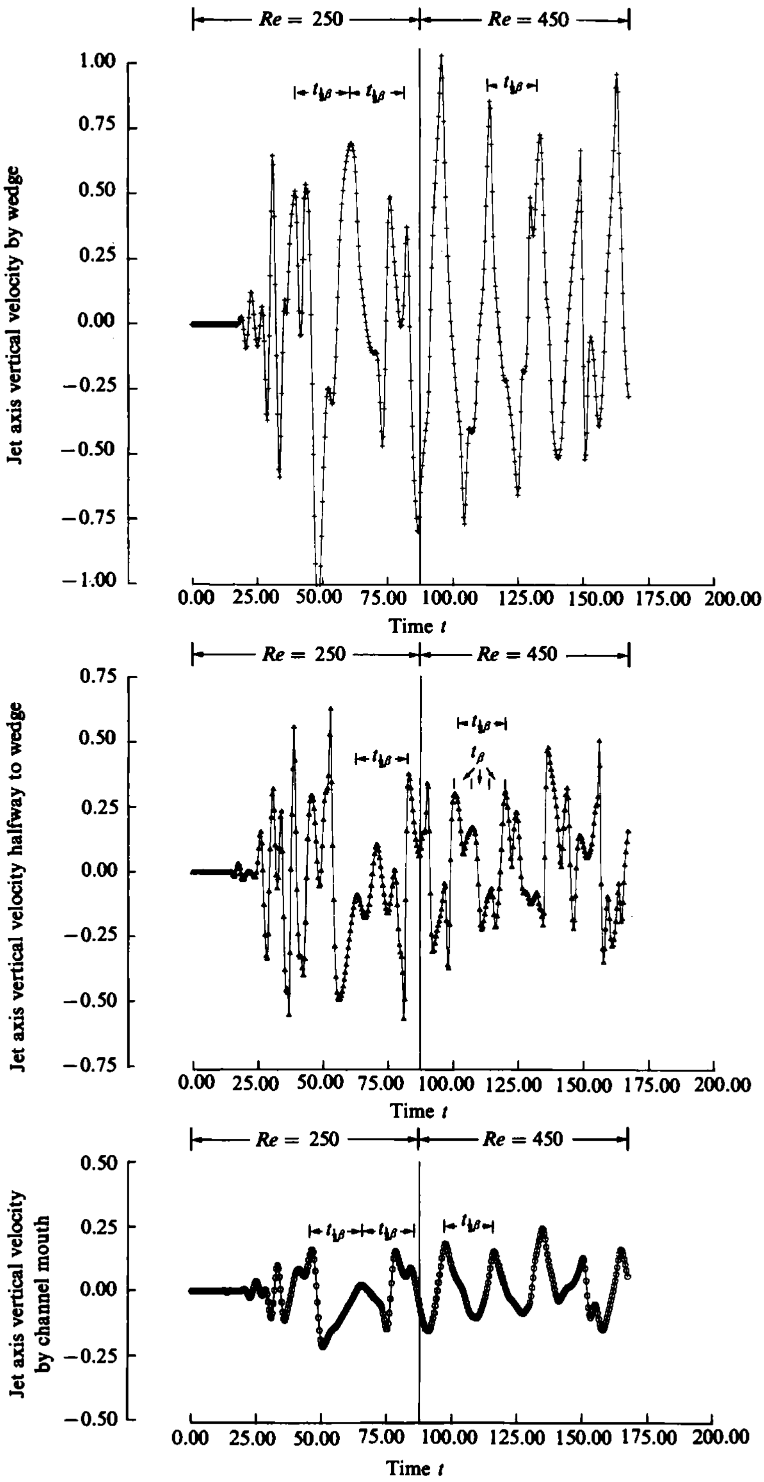

FIGURE 8. Transverse-velocity time histories at three locations along the jet centreline ($y = 0$) for $Re = 250$ and $Re = 450$ (from 250).

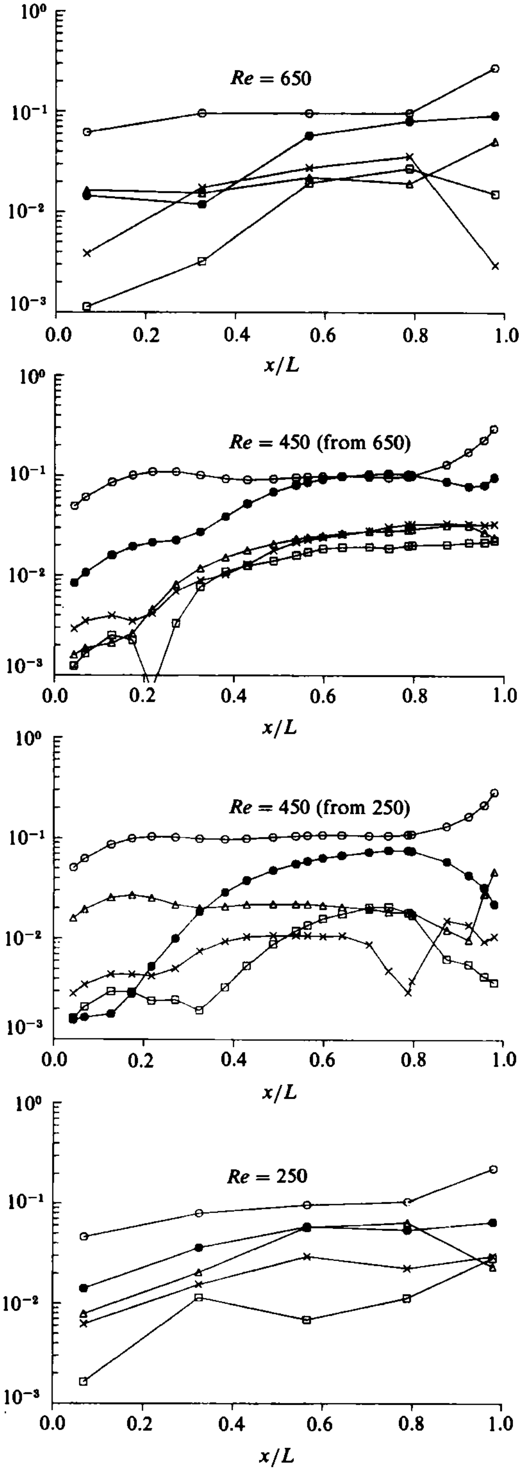

FIGURE 9. Growth of spectral-component amplitudes of the transverse velocity along the jet centreline ($y = 0$). (The components $\frac{1}{3}\beta$, $\frac{2}{3}\beta$, β, $\frac{4}{3}\beta$, and $\frac{5}{3}\beta$ are represented by the symbols, ○, △, ●, ×, and □, respectively.)

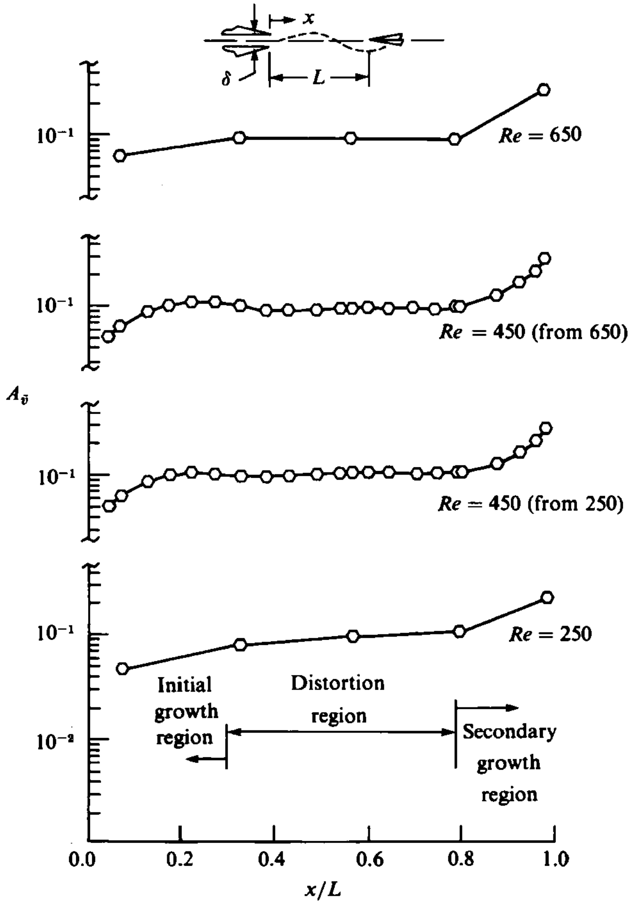

FIGURE 10. Growth of low-frequency modulating component $\frac{1}{3}\beta$ of transverse velocity along jet centreline ($y = 0$) for $Re = 650$, $Re = 450$ (from 650), $Re = 450$ (from 250) and $Re = 250$.

generally not as large as the β component for $Re = 450$ (from 650) for all x/L, which agrees with previous results regarding these two Re cases.

Figure 10 shows the amplitude growth of the low-frequency component $\frac{1}{3}\beta$. The persistence in shape of the amplitude distributions for all the *Re*-cases is quite remarkable. In all cases there is an initial growth region near the channel mouth and a secondary growth region near the wedge. The growth rates along the jet centreline are much the same for all *Re*-cases.

Figures 9 and 10 are in a format similar to figures found in LR. Although their *Re*-cases are somewhat different from those in this paper, the results, in general, compare quite favourably. It should be noted that their results are scaled by U_{c_L} the undisturbed horizontal Couette velocity component at $y = 0$, whereas results here are scaled by the mean Couette velocity U which is one-third smaller. Therefore, dimensionless amplitude results here are 50 % larger.

Figure 11 shows time-history traces of vorticity measured near to and away from the nozzle opening for the four Reynolds-number cases. Four traces have a value of zero and were measured at points 1 to 4 in figure 12(a) having (x, y) coordinates: $(-2.7437, \pm 3.2324)$, and $(-1.7784, \pm 2.2685)$. Four other traces were measured at points 5 to 8 in figure 12(a). These four locations were symmetrically placed (two on

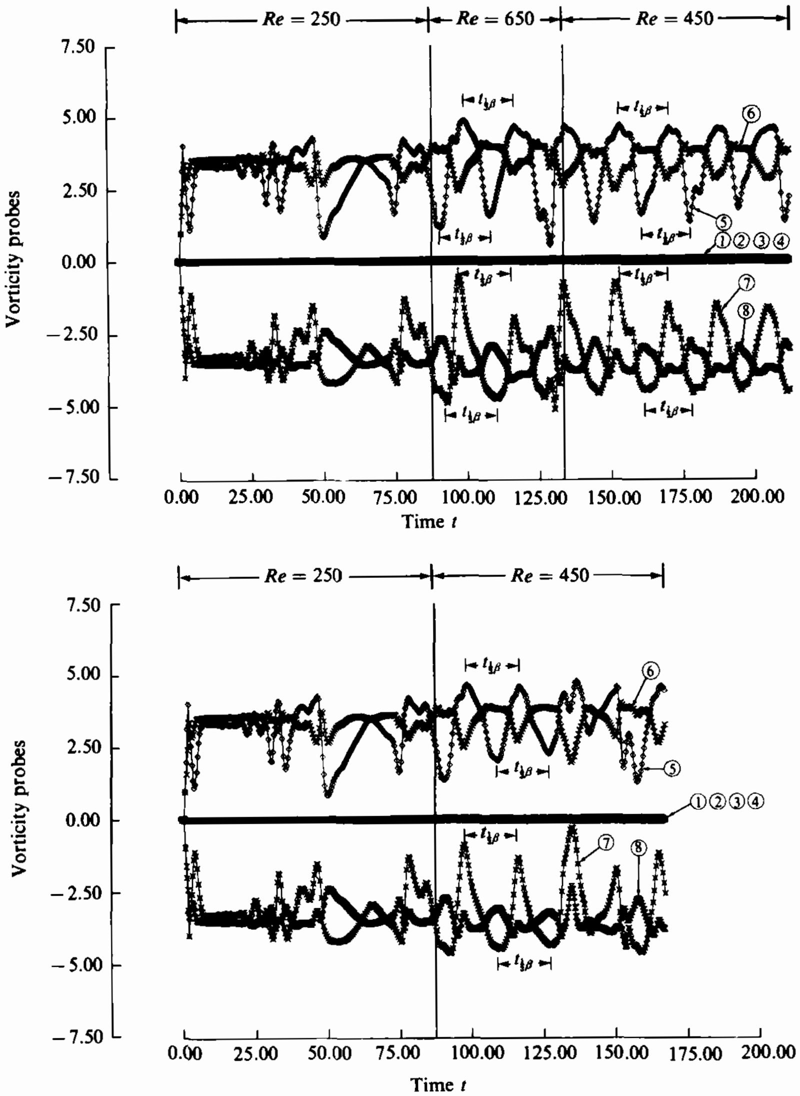

FIGURE 11. Vorticity time histories at selected locations near and away from the nozzle opening for $Re = 250, 650, 450$ (from 650), 450 (from 250). Point location, (x, y)-coordinates of point location, and plotting symbol for point locations 5 to 8 are, respectively, 5: (0.6850, 0.4375), ◇ ; 6: (0.7052, 0.3125), × ; 7: (0.6850, −0.4375), ⌑; 8: (0.7052, −0.3125), ⧗.

either side of the jet centre) within the jet just downstream of the nozzle opening. In general, the two positive traces measured at points 5 and 6 are antisymmetric to the two negative traces measured at 7 and 8, respectively, but with a phase shift of approximately $t_{\frac{1}{6}\beta}$, (i.e. when traces 5 and 6 are minimum in absolute value, 7 and 8 are maximum in absolute value). The dominant period of the traces is $t_{\frac{1}{3}\beta}$ as is expected.

4.3. *Numerical spectral results for wedge pressure, torque, and lift*

In figure 12(*b*) are shown the five locations 1 to 5 corresponding to the distances 0.0, 0.2475, 0.75, 1.5, and 3.0, respectively, measured along the lower wedge surface from the wedge tip where pressure time-history traces were obtained.

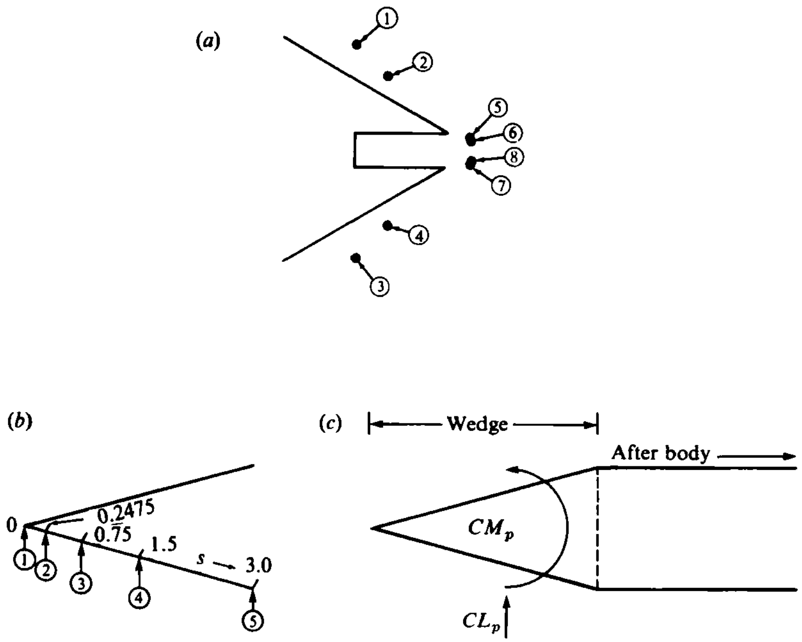

FIGURE 12. (*a*) Schematic drawing (drawn to scale) indicating locations of points 1 to 8 (for figure 11) in physical domain. (*b*) Locations 1 to 5 where wedge pressure time histories are taken. (*c*) Schematic drawing for torque CM_p and lift CL_p.

Figures 13–15 show, on the left, amplitudes of spectral components for the pressure traces which are shown on the right for $Re = 650$, $Re = 450$ (from 650), and $Re = 450$ (from 250), respectively. Spectral analysis for the upper wedge surface is the same as that of the lower. For all *Re*-cases the dominant component is $\frac{2}{3}\beta$. At the tip we expect $\frac{2}{3}\beta$ to be the dominant component because the pressure at the tip cannot discriminate between large-scale vortices that sweep upward or downward past the tip, so that, for example, the large-scale vortices associated with the $\frac{1}{3}\beta$ component (i.e. a^{ii}, a^{iv} in figure 3) on the upper or lower wedge surface produce a $\frac{2}{3}\beta$ component at the tip. The amplitude of the $\frac{2}{3}\beta$ component decreases slowly as the $\frac{1}{3}\beta$ component increases along the wedge surface moving away from tip in all the *Re* cases. This is particularly noticeable for $Re = 450$ (from 650) and $Re = 450$ (from 250). These results generally agree with that of Kaykayoglu & Rockwell for $Re = 600$ except that they find the component $\frac{2}{3}\beta$ decreasing much faster away from the tip so that the components $\frac{1}{3}\beta$ and β become dominant, with β then decreasing even further away from tip and $\frac{1}{3}\beta$ continuing to grow. The components $\frac{1}{3}\beta$ and β are expected to become dominant away from the tip since $\frac{1}{3}\beta$ is the frequency at which large-scale vortices (i.e. a^{ii} in figure 3) are swept away from the edge and β is the frequency at which vortices (i.e. b^{iii} in figure 3) pass along the surface of the edge. In the present results the β component does not stand out. (It should be remembered that the wedge-tip region is very sensitive numerically and experimentally.) The spectral results which most clearly show the expected dominance of the $\frac{2}{3}\beta$ and $\frac{1}{3}\beta$ components are obtained for $Re = 450$ (from 650) which also clearly shows the $\frac{4}{3}\beta$ component.

Figure 16 shows torque CM_p and lift CL_p (see figure 12*c*) time-history traces for the *Re* cases and figure 17 shows spectral-component amplitudes for these traces. The numerical integrations for CM_p and CL_p are performed along the complete extent

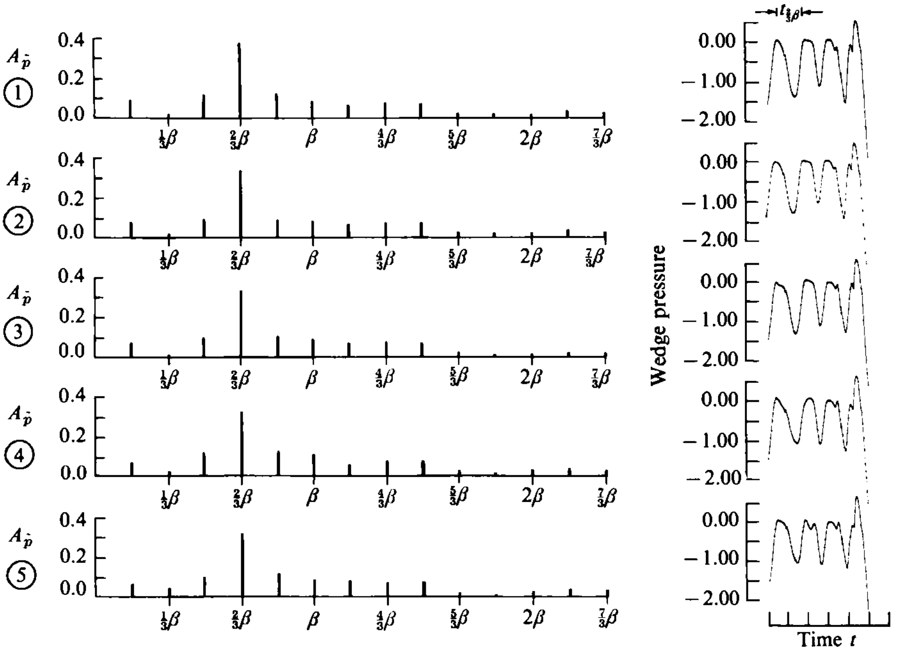

FIGURE 13. Spectral component amplitudes (on the left) for the corresponding wedge pressure time histories (on the right) at the five locations of figure 12(*b*) for $Re = 650$.

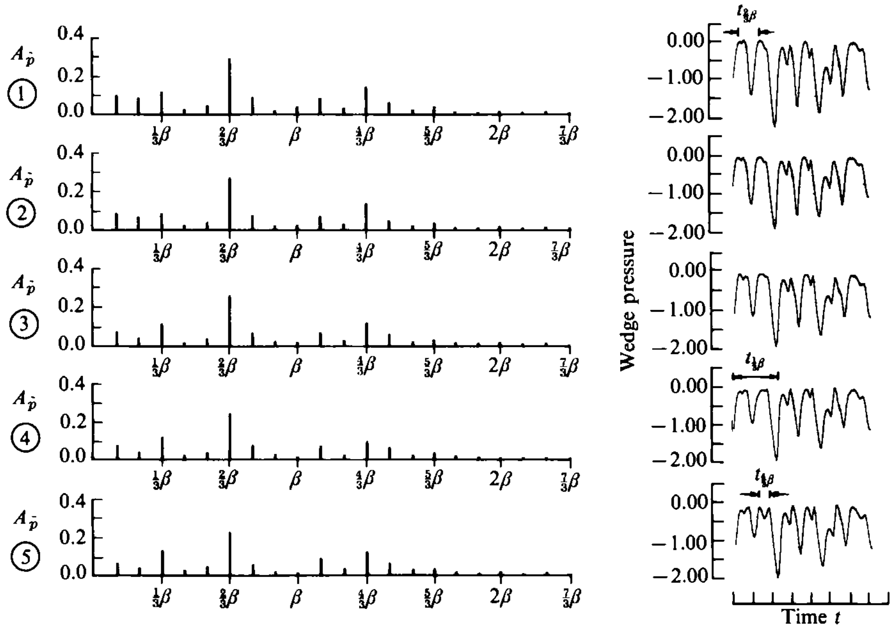

FIGURE 14. Same as figure 13 but for $Re = 450$ (from 650).

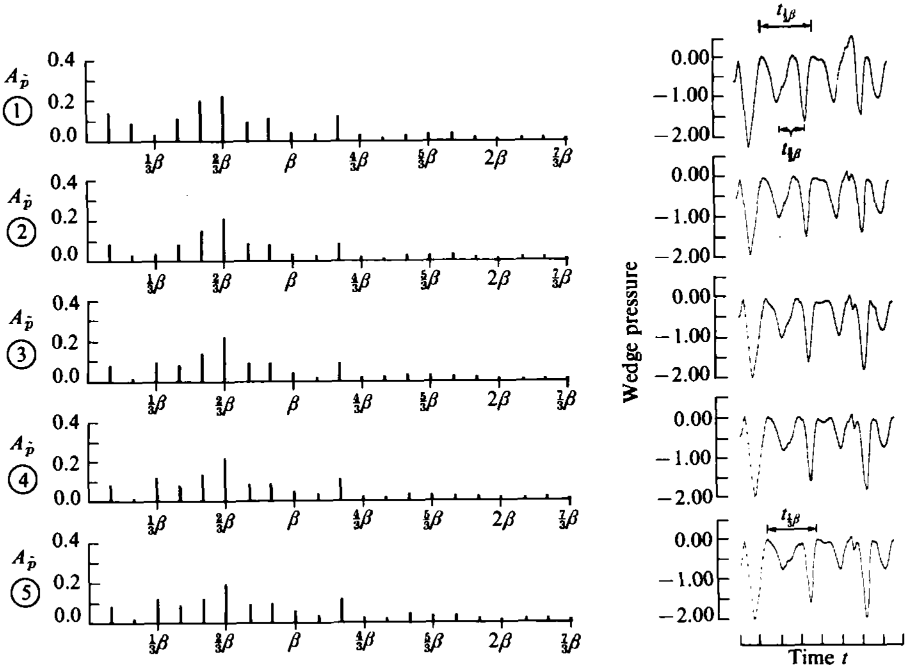

FIGURE 15. Same as figure 13 but for $Re = 450$ (from 250).

of the wedge surfaces only and not the afterbody (figure 12*c*). The wedge is the focus of attention and no numerical pressure evaluations were made on the afterbody. Presumably, the pressure time fluctuations downstream of the wedge along the afterbody die out since the flow there is nearly steady (see figure 6). Since CM_p and CL_p are given by integrals of the pressure (equations (8) and (9)), the $\frac{1}{3}\beta$ and β components are expected to dominate. The dominant component is $\frac{1}{3}\beta$ in all the Re cases. The β component, as expected, is also prominent especially for $Re = 650$ and $Re = 450$ (from 650). The case $Re = 450$ (from 650) once again has spectral results which show most clearly the expected dominance of the components $\frac{1}{3}\beta$, $\frac{2}{3}\beta$, β, and $\frac{4}{3}\beta$.

Table 1 (*a* and *b*) displays amplitudes of frequency components, which are at least 10% of the maximum amplitude, for the transverse-velocity time histories at $x/L = 0.7875$ and $y = 0$. Note in table 1 (*a*) the increase in the number of frequencies for $Re = 450$ (from 250) over that of $Re = 250$ which strongly suggests a partial jump to a stage II oscillation according to the criterion of LR. In table 1 (*b*) the number of frequencies is essentially maintained when going from $Re = 650$ to $Re = 450$ (from 650), strongly suggesting hysteresis at the stage II level. Note that the number of frequencies is greater in table 1 (*b*) than table 1 (*a*). Also note that the β component for $Re = 450$ (from 250) is substantially less than that of $Re = 450$ (from 650). These results agree with those concerning the visualization of $Re = 450$ (from 650) and $Re = 450$ (from 250) discussed earlier.

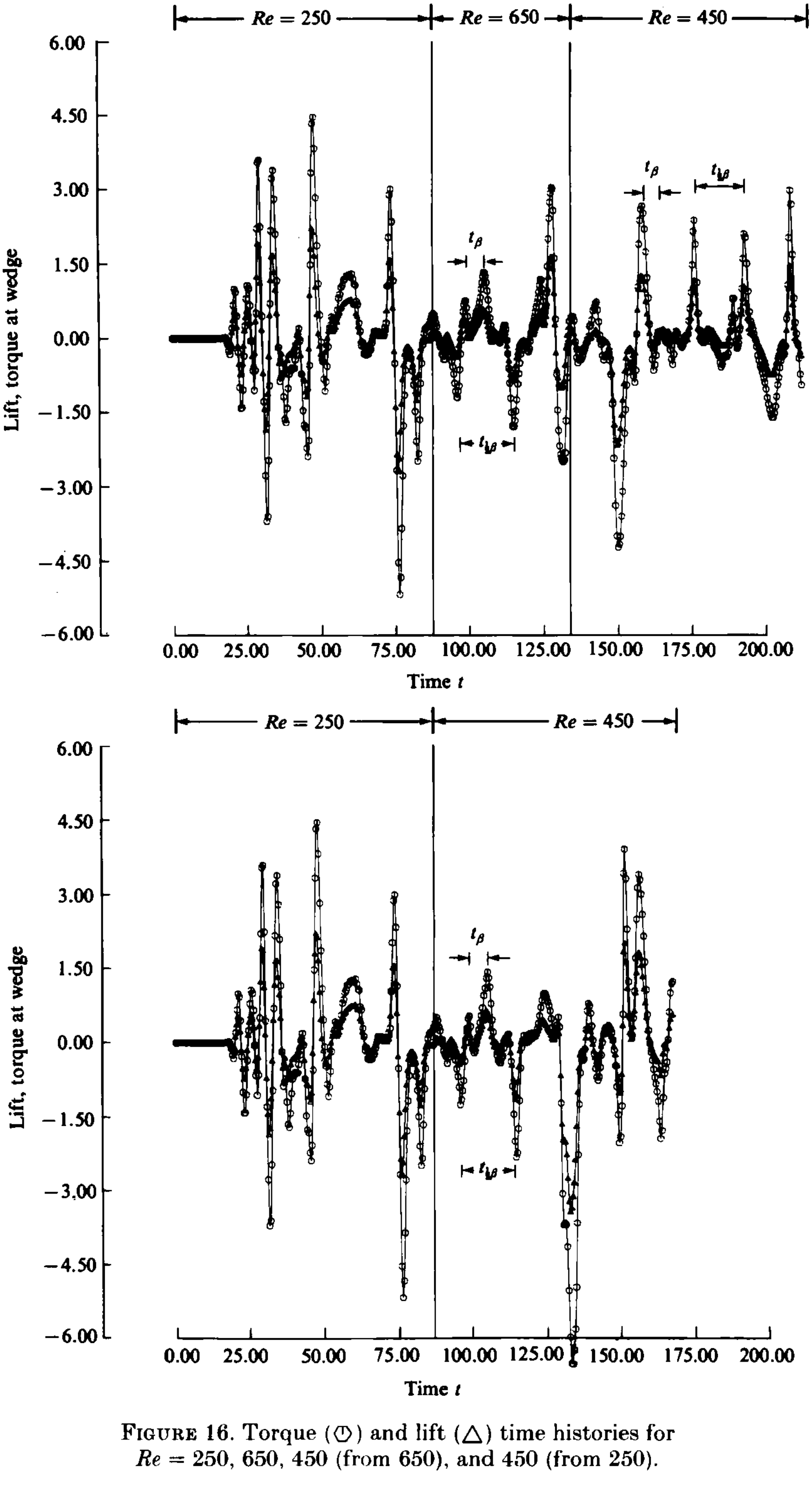

FIGURE 16. Torque (⦶) and lift (△) time histories for $Re = 250$, 650, 450 (from 650), and 450 (from 250).

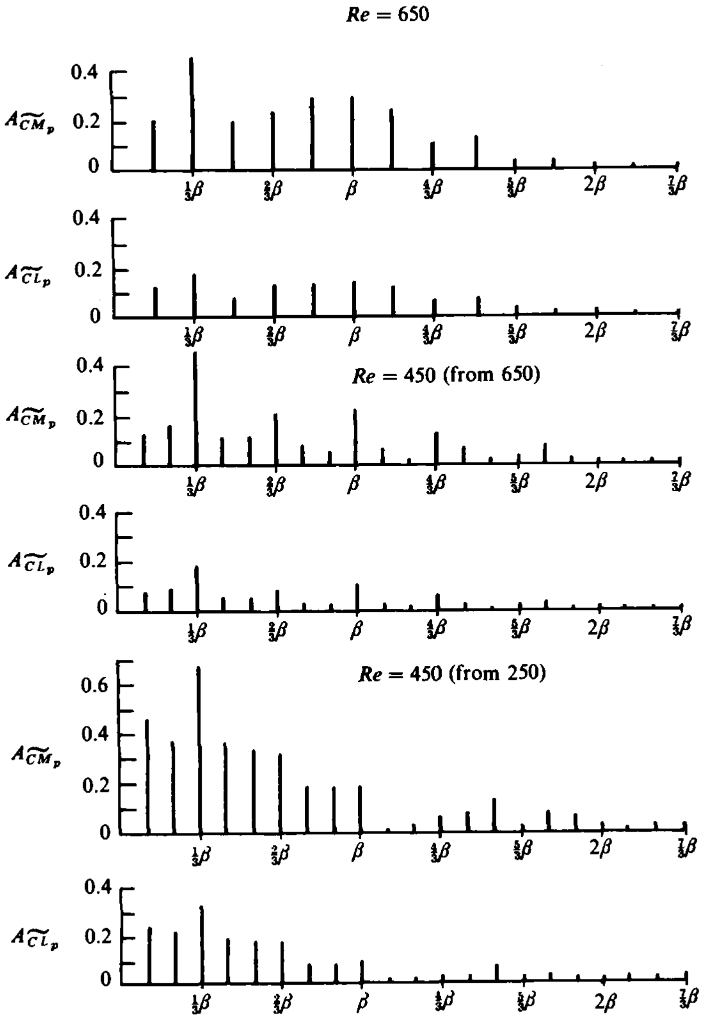

FIGURE 17. Spectral component amplitudes of the torque and lift traces of figure 16 for $Re = 650$, 450 (from 650), and $Re = 450$ (from 250).

5. Conclusions

A numerical computer-solution process has been used to calculate self-excited impinging jet flows. A vorticity/stream-function formulation has been used to solve the Navier–Stokes equations numerically, providing vorticity which is difficult to measure experimentally. The numerical solutions show the basic features of the oscillation cycle for both stage I (with the $\frac{1}{3}\beta$ component dominating) and stage II (with frequencies $\frac{1}{3}\beta$ and β dominating) oscillations. The main features are (*i*) growth of disturbances in the jet shear layer, (*ii*) formation of vortices near, and pressure fluctuations at, the surface of the wedge, (*iii*) upstream influence of this shear-layer–edge interaction to the sensitive region of the shear layer, and (*iv*) conversion of these perturbations to velocity fluctuations near the separation edge at the nozzle opening, allowing subsequent amplification in the downstream region of the shear layer.

The multi-frequency-component character of this class of unstable flows emerges

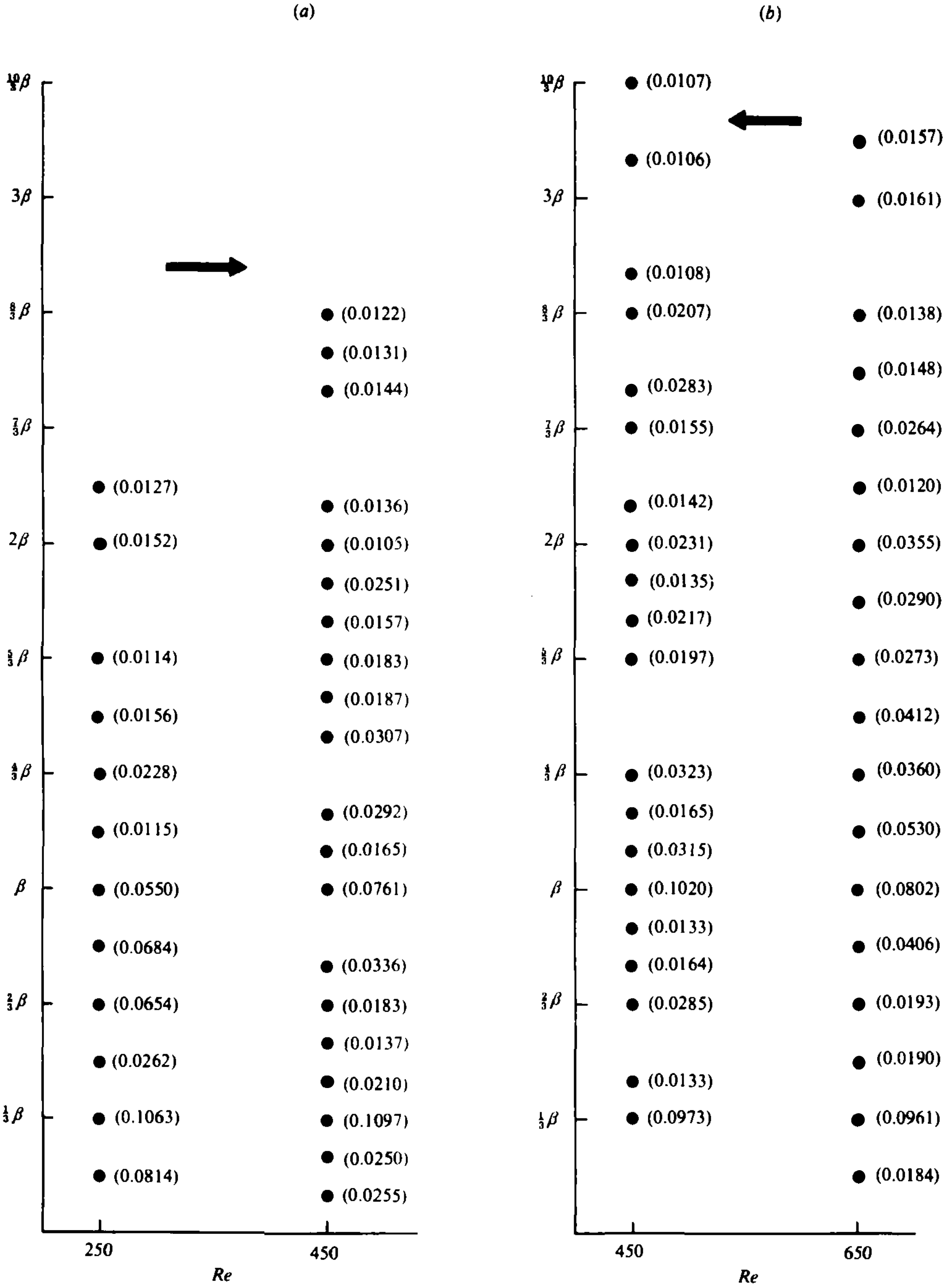

TABLE 1. (*a*) Multiple-frequency content of oscillating jet (v component) at $x/L = 0.7875$ on centreline ($y = 0$) indicating increase in number of spectral components (with amplitude of 10% of maximum amplitude) for $Re = 450$ (from 250) over that of $Re = 250$. (*b*) Multiple-frequency content of oscillating jet (v component) at $x/L = 0.7875$ on centreline ($y = 0$) indicating number of spectral components (with amplitude of 10% of maximum amplitude) is essentially unchanged for $Re = 450$ (from 650) as compared to $Re = 650$.

naturally from the numerical simulation, agreeing well with the corresponding experimental investigation of LR. These multiple frequency components are associated with nonlinear interaction between the fundamental instability frequency β of the jet, and a low-frequency modulation component $\frac{1}{3}\beta$. The fact that these two components, as well as other sum and difference frequencies, emerge from the calculation suggests that the numerical approach used in this paper could be employed in predicting the multi-frequency-component structure in a number of other free shear flows. Also of importance is the fact that these multi-frequency components arise from a two-dimensional rather than a three-dimensional instability of the planar jet. This may be the first time that this feature has been recognized, since most free-shear-layer experiments involving nonlinear instabilities include, by the very nature of the experiment, a degree of three-dimensionality. Only by numerical simulation, such as that brought forth in the present paper, can one conclusively ascertain the two-dimensionality of the mechanism.

The phenomena of frequency jumps and hysteresis has been considered with the numerical results in general agreement with those obtained experimentally, strongly indicating such effects.

Surface-wedge pressure has been calculated with results in general agreement with experiment.

Torque and lift calculations have been made and quite reasonable results have been obtained. Such quantities have not been measured experimentally.

Numerical flow computations provide a comparison with experimental results (neither of which are infallible). Agreement between the two approaches provides confidence for both methods. Moreover, the numerical computations can provide information on flow quantities such as vorticity which are very hard to obtain experimentally. With the cost of computer usage continually being reduced, the numerical approach will play an increasingly important role in providing such flow results.

The author wishes to thank Professor Don Rockwell of Lehigh University, Bethlehem, Pennsylvania, and Dr Hans Lugt of the David Taylor Naval Ship Research and Development Center, Bethesda, Maryland, for many valuable suggestions and discussions. The author would also like to thank the referees for their helpful comments.

REFERENCES

GOLDSTEIN, S. 1938 *Modern Developments in Fluid Dynamics*, vol. 1. Clarendon.

KAYKAYOGLU, R. & ROCKWELL, D. 1986 Unstable jet-edge interaction. Part II: Multiple frequency pressure fields. *J. Fluid Mech.* (to appear).

LUCAS, M. & ROCKWELL, D. 1984 Self-excited jet: upstream modulation and multiple frequencies. *J. Fluid Mech.* **147**, 333–352.

LUGT, H. J. & OHRING, S. 1975 Laminar flow behavior under slip-boundary conditions. *Phys. Fluids* **18**, 1–8.

MEHTA, U. B. & LAVAN, Z. 1975 Starting vortex, separation bubbles and stall: A numerical study of laminar, unsteady flow around an airfoil. *J. Fluid Mech.* **67**, 227–256.

NEWLAND, D. E. 1975 *An Introduction to Random Vibrations and Spectral Analysis*. Longman.

OHRING, S. 1983 Numerical solution of an impinging jet flow problem. *Proc. Fifth GAMM Conf. Rome 1983 Vieweg*, pp. 267–274.

PLANT, T. J. 1977 An exact velocity potential solution of steady, compressible flow over arbitrary, two-dimensional and axisymmetric bodies in simply connected fields. *AFFDL-TR-77-116*, Air Force Flight Dynamics Laboratory, Wright-Patterson Air Force Base.

POWELL, A. 1961 On the edgetone. *J. Acoust. Soc. Am.* **33**, 395–409.

ROCKWELL, D. 1983 Oscillations of impinging shear layers. *AIAA J.* **21**, no. 5, 645–664.

SOOD, D. R. & ELROD, H. G. 1974 Numerical solution of the incompressible Navier–Stokes equations in doubly-connected regions. *AIAA J.* **12**, 636–641.

SCHLICHTING, H. 1979 *Boundary-Layer Theory*, 7th edn., McGraw Hill.

THOMPSON, J. F., WARSI, Z. A. U. & MASTIN, C. W. 1982 Boundary-fitted coordinate systems for numerical solution of partial differential equations – a review. *J. Comp. Phys.* **47**, 1–108.

THOMPSON, J. F., THAMES, F. C., MASTIN, C. W. & SHANKS, S. P. 1975 Use of numerically generated body-fitted coordinate systems for solution of the Navier–Stokes equations. *AIAA Second Comp. Fluid Dyn. Conf., Hartford, Conn. 19–20 June.*